

# Advances in Monitoring Black Sea Dynamics: A New Multidecadal High-Resolution Reanalysis

Leonardo Lima<sup>1</sup>, Diana Azevedo<sup>1</sup>, Mehmet Ilicak<sup>2,1</sup>, Eric Jansen<sup>1</sup>, Filipe Costa<sup>1</sup>, Adil Sozer<sup>1,3</sup>, Pietro Miraglio<sup>1</sup>, Emanuela Clementi<sup>1</sup>

<sup>1</sup>CMCC Foundation – Euro-Mediterranean Center on Climate Change, Italy

<sup>2</sup>Eurasia Institute of Earth Sciences, Istanbul Technical University, Istanbul, Turkey

<sup>3</sup>Ordu University, Fatsa Faculty of Marine Science, Ordu, Turkey

Correspondence to: Leonardo Lima (leonardo.lima@cmcc.it)

**Abstract.** The Black Sea regional reanalysis serves as an essential tool for understanding the Black Sea’s response to climate variability and advancing regional ocean monitoring efforts. In particular, the Black Sea reanalysis (BLK-REA) is built with high spatial resolution, 1/40° horizontal grid and incorporating 121 vertical levels. The model implementation includes lateral open boundary conditions (LOBC) at the Marmara Sea, allowing more accurate inflow/outflow dynamics through the Bosphorus Strait. BLK-REA assimilates sea level anomaly (SLA) and in-situ observations and applies a heat flux correction via sea surface temperature relaxation. ~~The data assimilation system uses a background error covariance matrix evaluated through monthly EOFs over decadal periods to capture seasonal and decadal variability, and an observation-based mean dynamic topography is used for SLA assimilation. Enhancements in data assimilation (DA) include an improved background error covariance matrix and an observation-based mean dynamic topography for SLA assimilation.~~ When compared to available observations, the numerical results show high accuracy, with the largest temperature errors observed in the upper layers, primarily linked to the formation of the seasonal thermocline during the summer months. The SLA anomaly error is consistently around 0.02 m from the year 2000 onwards, and regions with elevated SLA errors are closely associated with the Rim Current and its mesoscale variability. Furthermore, BLK-REA plays a crucial role in generating Ocean Monitoring Indicators, which are essential for tracking and assessing the impacts of climate change in the Black Sea. For example, temperature data indicate ongoing warming in the 25 to 150 m layer, where the Cold Intermediate Layer is located. ~~In addition, the Black Sea meridional overturning circulation has decreased from 0.1 Sv in 1993 to approximately 0.01 Sv in 2010, highlighting significant changes in the basin's circulation.~~ The system is regularly updated, with the next version expected to improve both the model and DA components. For a future perspective, the next BLK-REA will expand the domain to include the Azov Sea and will feature an enhanced Bosphorus LOBC.

## 29 1 Introduction

30 The Black Sea is a semi-enclosed basin linked to the Marmara Sea through the Bosphorus Strait, the narrowest part of the  
31 Turkish Strait System (TSS). The TSS continues through the Dardanelles Strait, which connects the Marmara Sea to the  
32 Mediterranean. Salty waters originating from the Mediterranean Sea flow into the Black Sea through the TSS, serving as its  
33 main source of salinity. Despite this influx of saltier waters, the Black Sea is mainly considered a freshwater basin,  
34 characterized by a negative balance between evaporation ( $E$ ), precipitation ( $P$ ), and runoff ( $R$ ):  $E - P - R$ . This imbalance  
35 is compensated by a two-layer exchange through the Bosphorus Strait, where a stronger flow of the fresher upper layer moves  
36 southward toward the Marmara Sea (Beşiktepe et al., 1994; Altiok and Kayışoğlu, 2015). The surface circulation in the Black  
37 Sea is primarily driven by the Rim Current, a semi-permanent cyclonic (counterclockwise) jet that flows along the edges of  
38 the basin. Along its path, this current interacts with multiple cyclonic gyres within its core and anticyclonic (clockwise) eddies  
39 along its peripheries, such as the Batumi and Sevastopol eddies (Oguz et al., 1993; Korotaev et al., 2003).

40 An important feature of the Black Sea is the Cold Intermediate Layer (CIL), a cold water mass generated each winter through  
41 surface cooling and convective mixing. The CIL helps the ventilation of the sub-surface of the Black Sea (Özsoy and Ünlüata,  
42 1997). ~~The CIL and~~ is typically defined by water temperatures below  $8^{\circ}\text{C}$  and extends between depths of 30 m to 80 m (Ivanov  
43 et al., 2001). The formation of the CIL in the Black Sea is primarily driven by convective processes during cold winters, where  
44 cool surface waters become denser and sink to intermediate depths. Recent studies have emphasized that CIL variability is not  
45 solely controlled by local winter conditions but is the result of a complex interplay between atmospheric forcing, lateral  
46 advection, and oceanic circulation (Korotaev et al., 2014; Miladinova et al., 2018; Capet et al., 2020). For example, the Rim  
47 Current and associated mesoscale eddies create localized upwelling and downwelling regions, influencing the CIL distribution  
48 (Podymov et al., 2023).

49 Understanding the circulation and physical processes of the Black Sea from the past to recent years can be supported by ocean  
50 reanalyses. These products use state-of-the-art models driven by atmospheric forcing and data assimilation,  
51 which integrates high-quality multi-year satellite and in situ datasets to reconstruct historical ocean conditions (Haines et al.,  
52 2018; Yang et al., 2025). ~~Ocean reanalyses utilize state-of-the-art models that are constrained by atmospheric forcing and~~  
53 ~~incorporate the best available observations through data assimilation techniques to reconstruct historical conditions.~~ These  
54 products are crucial for monitoring, as they provide insight into the ocean's evolution in response to external forcing, and they  
55 allow for the assessment of how environmental changes may affect marine biota, ecosystems, and activities dependent on the  
56 health of marine environments.

57 This work presents a new high-resolution Black Sea reanalysis (hereafter referred to as BLK-REA), developed within the  
58 Copernicus Marine Service, which updates the model components and the variational data assimilation system, assimilating  
59 both in situ and satellite observations to provide a consistent reconstruction of the Black Sea's physical state. BLK-REA  
60 incorporates improved lateral open boundary conditions to better represent exchange flows through the Bosphorus Strait, an  
61 improved freshwater budget, and a high-resolution model configuration that allows better representation of mesoscale and

62 submesoscale processes. Assimilation of satellite and in situ datasets ensures that the reconstructed historical ocean state is  
63 physically consistent and captures the evolution of key monitoring indicators for the Black Sea.  
64 ~~-Previous Black Sea reanalyses, also developed within the framework of the Copernicus Marine Service, have served as~~  
65 ~~valuable tools for improving our understanding of the Black Sea's response to climate change. For example, they revealed a~~  
66 ~~recent warming of the Black Sea's surface, observed in both sea surface temperature (SST) and subsurface temperature (Mulet~~  
67 ~~et al., 2018; Lima et al., 2021).The Black Sea reanalysis, developed within the framework of the Copernicus Marine Service,~~  
68 ~~has been a valuable tool for enhancing our understanding of the Black Sea's response to climate change. For instance, its results~~  
69 ~~demonstrated a recent surface warming of the Black Sea, identified through both sea surface temperature (SST) and subsurface~~  
70 ~~temperature (Mulet et al., 2018; Lima et al., 2021).~~ An ocean monitoring indicator (OMI) based on ocean heat content (OHC)  
71 in the upper 300 m has also shown warming in the Black Sea. This increasing trend, as indicated by both reanalysis data and  
72 temperature measurements from Argo floats (Lima et al., 2020; Stanev et al., 2019), has contributed to the reduced presence  
73 of the CIL in the Black Sea in recent years.

74 Beyond OHC, Black Sea reanalysis has served as the foundation for other OMIs also produced within the scope of the  
75 Copernicus Marine Service. Using its velocity fields, Peneva et al. (2021) created an index for the Rim Current, showing that  
76 the annual mean current speed fluctuated by approximately 30% between 1993 and 2019, with a positive trend of about 0.1 m  
77 s<sup>-1</sup> per decade. Ilicak et al. (2022) analyzed the meridional overturning circulation in the Black Sea and identified a strong  
78 correlation between the CIL and a newly proposed index representing the maximum overturning circulation in density space.  
79 Gunduz et al. (2021) proposed an index to characterize the upwelling system along the Turkish coast. Their study revealed  
80 significant year-to-year variations in upwelling intensity and duration, driven primarily by wind patterns. In addition, they also  
81 found that recent declines in the CIL may have further influenced the properties of the upwelled waters.

82 Additionally, Black Sea reanalysis has played an important role in the practical development of the Black Sea physics forecast  
83 system (Ciliberti et al., 2022) and, more recently, in generating hourly datasets of velocity components and sea surface height  
84 for driving wave reanalysis within the framework of the Black Sea Monitoring and Forecasting Centre (BLK-MFC) under the  
85 Copernicus Marine Service (Ciliberti et al., 2021). One of the main challenges in developing a reanalysis for the Black Sea is  
86 the scarcity of in-situ observational data to be assimilated, particularly in certain periods, such as the 1990s. This data scarcity  
87 is even more pronounced in deeper layers. The absence of observational data requires the use of a robust model capable of  
88 accurately simulating the physical processes involved in the Black Sea. Thus, significant progress has been made in improving  
89 the quality of the BLK-REA model component with respect to its previous version, including the implementation of a new  
90 configuration with lateral open boundary conditions (LOBCs) to better simulate exchange flows through the Bosphorus Strait,  
91 such as the inflow of saltwater from the Marmara Sea. Also, the freshwater balance in the model has been refined by  
92 incorporating atmospheric forcing with hourly precipitation data, alongside monthly measurements of the Danube River  
93 discharge.

94 These improvements emphasize the importance of developing a regional reanalysis that integrates specific configurations and  
95 physical parameterizations tailored to accurately represent the unique characteristics of the Black Sea, which is challenging to

96 achieve with global reanalyses. The latter often rely on fixed parameter adjustments optimized for other regions in the global  
97 ocean. In addition, a regional reanalysis typically utilizes higher-resolution models, allowing for a more accurate representation  
98 of mesoscale and submesoscale processes, which are often unresolved or only partially captured by the coarse resolution of  
99 current global reanalyses.

100 This article is organized as follows: Section 2 provides a detailed description of ~~the BLK-REA configuration for the new Black~~  
101 ~~Sea reanalysis (hereafter referred to as BLK-REA)~~, which was released in December 2024. ~~Section 3 presents the main BLK-~~  
102 ~~REA results and their validation, as well as the updated OMIs for the Black Sea based on BLK-REA.~~ ~~Section 3 discusses its~~  
103 ~~main results.~~ Finally, Section 4 summarizes ~~the key findings and outlines improvements and data needs for future versions~~  
104 ~~conclusions.~~

## 105 **2 Methodology**

106 Most of the methodology and configurations follow the previous Black Sea Reanalysis version (Lima et al., 2021), such that  
107 this section focuses on the main changes and enhancements present in the newly released version.

### 108 **2.1 Ocean Model**

109 The BLK-REA model component is the Nucleus for European Modelling of the Ocean (NEMO version 4.0, Madec and the  
110 Nemo team, 2019) configured for the domain (Azov and Marmara Seas are not included). NEMO is implemented at a  
111 horizontal resolution of  $1/40^\circ$  and 121 vertical geopotential levels. This horizontal resolution provides a spatial discretization  
112 of approximately 2.5 km, which conforms to the mesoscale eddy-resolving scale; the Rossby radius of deformation in the  
113 Black Sea is approximately 20 km. The model is driven by atmospheric fluxes derived from ECMWF ERA5 reanalysis with  
114 spatial and temporal resolutions of  $1/4^\circ$  and 1 hour, respectively. The atmospheric forcing considers the following variables:  
115 components of 10-m wind, total cloud cover, 2-m air temperature, 2-m dew point temperature, mean sea level pressure and  
116 precipitation. The system computes momentum, heat, and water fluxes at the air-sea interface using bulk formulae originally  
117 developed for the Mediterranean Sea (Castellari et al., 1998; Pettenuzzo et al., 2010), which have also been employed in other  
118 Black Sea systems (Ciliberti et al., 2022; Lima et al., 2021). Additionally, the system applies daily sea surface temperature  
119 relaxation for heat flux corrections based on the ESA-CCI SST-L4 product (Good et al., 2020).

#### 120 **2.1.1 Lateral open boundary conditions**

121 One of the key challenges in modeling the Black Sea dynamics is accurately simulating the outflow and inflow through the  
122 Bosphorus Strait. This is essential for correctly representing the surface and intermediate depth salinity patterns and sea surface  
123 height (SSH) trends, as the Bosphorus acts as the sole passage for saltwater entering the Black Sea, and the only exit of the  
124 surface Black Sea water. The previous Black Sea reanalysis approach applied closed boundary conditions, requiring  
125 temperature and salinity restoration to achieve more accurate results. Additionally, SSH was controlled by treating the

126 Bosphorus as an inverse river with a controlled flow to prevent artificial SSH trends. The present version incorporates open  
127 boundaries, using results from the Unstructured Turkish Straits System (U-TSS) model (Ilicak et al., 2021), leading to a more  
128 accurate representation of these dynamics. U-TSS is built upon the Shallow Water Hydrodynamic Finite Element Model  
129 (SHYFEM; Micalletto et al., 2022). SHYFEM employs an unstructured finite element grid in the horizontal dimension and  
130 assumes hydrostatic approximation, solving depth-integrated shallow water equations in the vertical. The model features a  
131 horizontal resolution ranging from 500 meters in deeper regions to 50 meters in shallower areas, enabling a detailed  
132 representation of the Turkish Straits: Dardanelles and Bosphorus. Additionally, it incorporates 93 geopotential coordinate  
133 levels in the vertical dimension. The current reanalysis simulation utilizes LOBCs from monthly-averaged fields of  
134 temperature, salinity, U and V velocity components, and SSH from a 4-year U-TSS simulation covering the period 2016–2019.  
135 Flather’s boundary condition is applied to the barotropic component, while the flow relaxation scheme is utilized for tracers  
136 and baroclinic components, as implemented in NEMO. Custom interfaces between U-TSS and BLK-REA have been developed  
137 to adapt the U-TSS model outputs for the BDY module in NEMO (Chanut, 2005).

138 Due to computational constraints, the LOBCs at the Bosphorus Strait were derived from monthly-averaged outputs of a U-  
139 TSS simulation covering the period 2016–2019. A monthly climatology from this period was applied consistently over the full  
140 reanalysis timeline (1993–2022) to represent seasonal variability. Although this approach does not capture interannual signals  
141 at the boundary, the internal dynamics of the Black Sea, combined with the data assimilation of satellite and in situ  
142 observations, help maintain physical consistency throughout the basin.

## 143 **2.2 Observations**

144 The system assimilates sea level anomaly (SLA) data from the dataset European Seas Along-Track L3 Sea Surface Heights  
145 Reprocessed, Tailored for Data Assimilation, available in the Copernicus Marine Service catalog  
146 (SEALEVEL\_EUR\_PHY\_L3\_MY\_008\_061, <https://doi.org/10.48670/moi-00139>; Faugère et al., 2022). To maximize the  
147 number and spatial coverage of in-situ observations assimilated into the model, we combine multiple datasets using a  
148 predefined priority order, ensuring that duplicate profiles are excluded, as follows:

- 149 1. Global Ocean CORA In-situ Observations – Yearly Delivery in Delayed Mode from Copernicus Marine Service  
150 (INSITU\_GLO\_PHY\_TS\_DISCRETE\_MY\_013\_001; <https://doi.org/10.17882/46219>) (Szekely et al., 2024).
- 151 2. Global Ocean In-situ Near-Real-Time Observations from Copernicus Marine  
152 Service (INSITU\_GLO\_PHYBGCWAV\_DISCRETE\_MYNRT\_013\_030; <https://doi.org/10.48670/moi-00036>).
- 153 3. SeaDataNet historical in-situ data collections (Myroshnychenko and Simoncelli, 2018; Myroshnychenko, 2020).

154  
155 In data assimilation, the in situ instrumental errors assume different values for T and S and vary in the vertical dimension based  
156 on statistics derived from Ingleby and Huddleston (2007). The in-situ representation errors are defined as a multiplicative  
157 factor applied to the depth-dependent instrumental errors and vary horizontally on the model grid according to previous model-  
158 observation statistics. In this component, the same spatially varying factor is applied to T and S, which is a simplification

159 justified by the similar spatial sampling patterns and statistical structure of the T/S in situ observational datasets. Representation  
160 errors account for unresolved physical processes, subgrid-scale variability, and model errors that are not part of instrumental  
161 uncertainties. Both components of in situ errors are kept constant over time. For SLA observations, the instrumental error is  
162 set to 4 cm, and the representation errors vary spatially and monthly following Oke and Sakov (2008). Similar to the previous  
163 version, a background quality check is implemented in the data assimilation system to reject observations that deviate  
164 significantly from the model prior solution. Rejection by background quality control does not necessarily indicate erroneous  
165 data, but often reflects large innovations that would otherwise introduce undesirable shocks in the model state. The quality  
166 control procedures and data rejection thresholds are applied as described in Lima et al. (2021), with no changes introduced in  
167 BLK-REA. In data assimilation, the in-situ instrumental errors for temperature and salinity are depth-dependent, based on  
168 statistics from Ingleby and Huddleston (2007), while the in-situ representation errors are horizontally variable on the model  
169 grid, derived from previous model-observation statistics, and use same values for T and S. Both error components remain  
170 constant over time. For SLA observations, the instrumental error is fixed at 4 cm, while representation errors vary spatially  
171 and monthly, following Oke and Sakov (2008). Similar to the previous version, a background quality check is implemented in  
172 the data assimilation model to reject observations that deviate significantly from the model prior solution.  
173 In contrast to the previous version of the reanalysis (Lima et al., 2021), which used a model-derived mean dynamic topography  
174 (MDT), An-an enhancement in the present version is the use of an observation-based mean dynamic topography (MDT) to  
175 compute the model-equivalent SLA in data assimilation. Sensitivity tests indicated that this choice improves the assimilation  
176 skill of SLA, leading to systematically reduced RMSD values. The observation-based MDT field is available in the Copernicus  
177 Marine Service catalog: <https://doi.org/10.48670/moi-00138>.

### 178 **2.3 Data Assimilation**

179 The data assimilation system, OceanVar, utilizes a three-dimensional variational (3D-Var) assimilation algorithm. OceanVar  
180 was initially developed for the Mediterranean Sea (Dobricic and Pinardi, 2008) and subsequently extended to the global ocean  
181 (Storto et al., 2011) and Black Sea (Ciliberti et al., 2022; Lima et al., 2021). The new system utilizes OceanVar, following the  
182 same equations outlined in Lima et al. (2021), with particular emphasis on the cost function ( $J$ ) equation presented as follows:

$$183 \quad J = \frac{1}{2} \delta x^T B^{-1} \delta x + \frac{1}{2} (H \delta x - d)^T R^{-1} (H \delta x - d) \quad (1)$$

184 where  $\delta x = x_a - x_b$  is the increment, i.e., the difference between the analysis ( $x_a$ ) and background ( $x_b$ ),  $d = y - H(x_b)$  is  
185 the misfit between an observation vector  $y$  and its modeled correspondent (in the observation space) where  $H$ , the observation  
186 operator, maps the model fields to the observation locations. OceanVar is a multivariate scheme, i.e., the state vector  $x$  can  
187 contain the following model state variables: T, S, SLA, and horizontal velocities ( $u$  and  $v$ ). However, only the first three  
188 variables are employed in the present BLK-REA implementation.  $B$  and  $R$  are respectively the background and observation  
189 covariance matrices.  $R$  is diagonal in the observation space and includes the sum of instrumental and representation errors,

190 along with an additional error component that depends on the time difference between each observation and the analysis time.  
191 The latter component is weighted according to this temporal distance.

192 In OceanVar, the variational cost function is solved using the incremental formulation (Courtier, 1997), with preconditioning  
193 of the cost function minimization achieved through a change-of-variable transformation. Thus, to avoid inverting the  $B$  matrix  
194 and to precondition the minimization of the cost function, the  $B$  matrix is defined as  $B = VV^T$  where  $V$  is decomposed into a  
195 sequence of linear operators:  $V = V_\eta V_h V_v$ . The  $V$  operator represents the background error covariance matrix, capturing the  
196 interdependencies among variables. Furthermore, a new control variable,  $v = V^+x$  (and thereby  $x = Vv$ ), is introduced for the  
197 minimization process through the application of a transformation. Thus Eq (1) becomes:

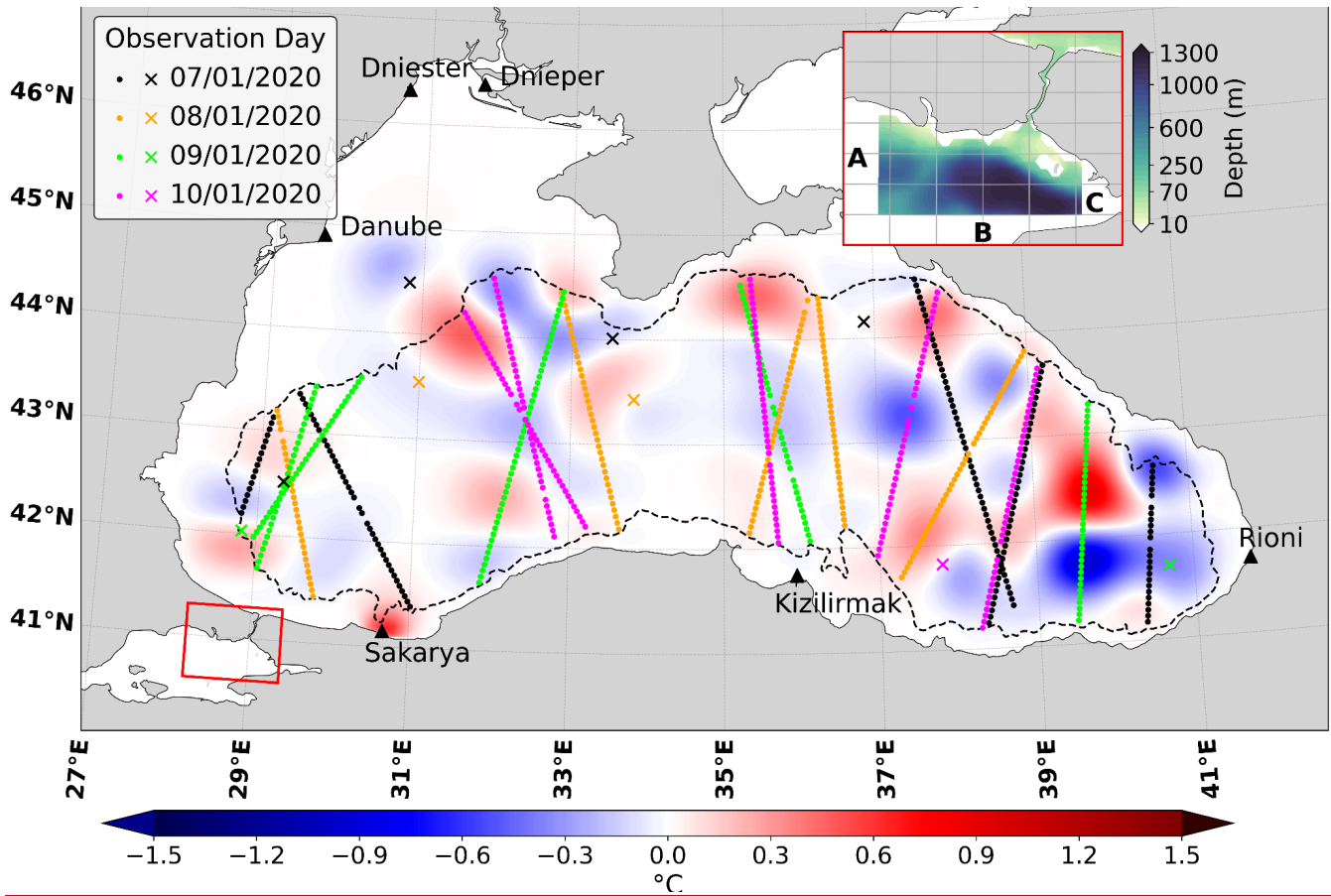
$$198 \quad J = \frac{1}{2}v^T v + \frac{1}{2}(HVv - d)^T R^{-1}(HVv - d) \quad (2)$$

199

200 In the present version, the linear operators  $V_\eta$  and  $V_h$  follow the same formulation described by Lima et al. (2021). The dynamic  
201 height operator in  $V_\eta$  imposes local hydrostatic and geostrophic balance among SLA, temperature, and salinity increments,  
202 following Storto et al. (2011), with a level of no motion assumed at 1000 m, where this balance is valid. This restricts SLA  
203 assimilation to deep-water regions.  $V_h$  represents horizontal correlations, modeled with a first-order recursive filter (Farina et  
204 al., 2015) and a fixed correlation length-scale of 20 km. Instead,  $V_v$  incorporates background-error T and S vertical covariances  
205 that are modelled through 45-mode multivariate Empirical Orthogonal Functions (EOFs) and derives from a previous  
206 integration including the assimilation of SLA, T and S profiles, using the full model resolution. In addition, the new approach  
207 is non-stationary and a different set of EOFs are applied considering the following decades: 1984–1993, 1994–2003, 2004–  
208 2013, and 2011–2020. EOFs are calculated for each month from anomalies estimated from daily T, S and SSH fields with  
209 respect to the long-term monthly mean of the corresponding decade.

## 210 **2.4 Strategies and experiment setup**

211 The experiment is initialized in 1991 with a rest state of temperature and salinity fields derived from the World Ocean Atlas  
212 climatology (WOA 2018, Garcia et al., 2019). Following a spin-up of 2 years (1991-1992), the BLK-REA starts in 1993. The  
213 data assimilation is applied every 2 days, i.e., if the model initializes at time  $t$ , the next data assimilation cycle is performed at  
214 the time  $t + 2$ . The observation window is 4 days centered at the analysis time, so that each cycle assimilates observations  
215 from 2 days before until 2 days after the analysis time. Figure 1 shows SST increments (in °C) over the Black Sea on 09  
216 January 2020, overlapped with along-track SLA and in situ profile data assimilated during a single DA cycle in the BLK-REA.  
217 The subplot highlights the Marmara Box and its bathymetry, where boundary conditions from U-TSS are applied along faces  
218 A, B, and C. In the Black Sea, the limited availability of in-situ observations for assimilation leads to systematic errors in  
219 certain variables during specific periods, particularly in the deeper layers. To mitigate this bias, large-scale bias correction  
220 (LSBC) toward WOA2018 decadal climatologies is applied below 700 meters. The formulation and additional details on the  
221 LSBC scheme are described in Lima et al. (2021).



222 **Figure 1: SST increments (in °C) over the Black Sea on 09 January 2020, shown with a blue–white–red color scale. Triangles mark**  
 223 **the positions of the main river inflows, while along-track SLA observations and in situ profile data (mostly Argo floats during this**  
 224 **period; showing their positions as ×) are also displayed. Each color corresponds to a different day within a 4-day observation window**  
 225 **centered at 00:00 UTC on 09 January 2020. The subplot highlights the Marmara Box (red rectangle) and its corresponding**  
 226 **bathymetry, where boundary conditions from U-TSS are prescribed along faces A, B, and C. No assimilation is performed inside**  
 227 **the Marmara Sea, and thus the SST increments there are zero.**  
 228

229 **3 Results and discussion**

230 This section presents validations of key variables from the BLK-REA. The validations are quasi-independent, as they consider  
 231 ~~This section presents quasi-independent validations of key variables from the BLK-REA, which consider~~ both assimilated  
 232 observations and those excluded during the data assimilation process due to specific adjustments (e.g., background quality  
 233 control). Additionally, it provides results for a set of OMIs computed from the BLK-REA.

234 **3.1 Validation**

235 Spatial seasonal maps of reanalysis SST are compared to satellite data in the period 1993-2022 and their difference shows a  
 236 predominance of model negative biases in winter and spring, and positive biases in summer and fall, with a few exceptions as

237 follows (Figure 24; left). Positive values of 0.1°C up to 0.3°C are visible in some regions during winter, such as close to the  
 238 Danube river mouth and along the southwest coast. Negative biases are present adjacent to the Kerch Strait, and the lowest  
 239 negative biases, of more than 1.0°C, are exhibited in the upwelling region along the western Anatolian coast in summer. Most  
 240 of the central-eastern area is covered by negative bias in fall. SST RMSD (Root Mean Squared Difference) maps indicate that  
 241 errors are generally lower in spring and higher in fall (Figure 24; right). In general, larger values can be seen close to large  
 242 river mouths such as near the Dnieper in winter and Danube in winter, spring, and summer. The highest errors, exceeding 1°C,  
 243 are observed along the western Anatolian Turkish coast in both summer and fall. In this region, a similar overestimation of  
 244 upwelling phenomena was observed in the results of the previous Black Sea reanalysis, which was attributed to the influence  
 245 of stronger winds (Lima et al., 2021). Recent analyses have indicated that the air-sea bulk formulation may be responsible for  
 246 the intensified upwelling, and we plan to refine this model component in future releases of the Black Sea reanalysis.

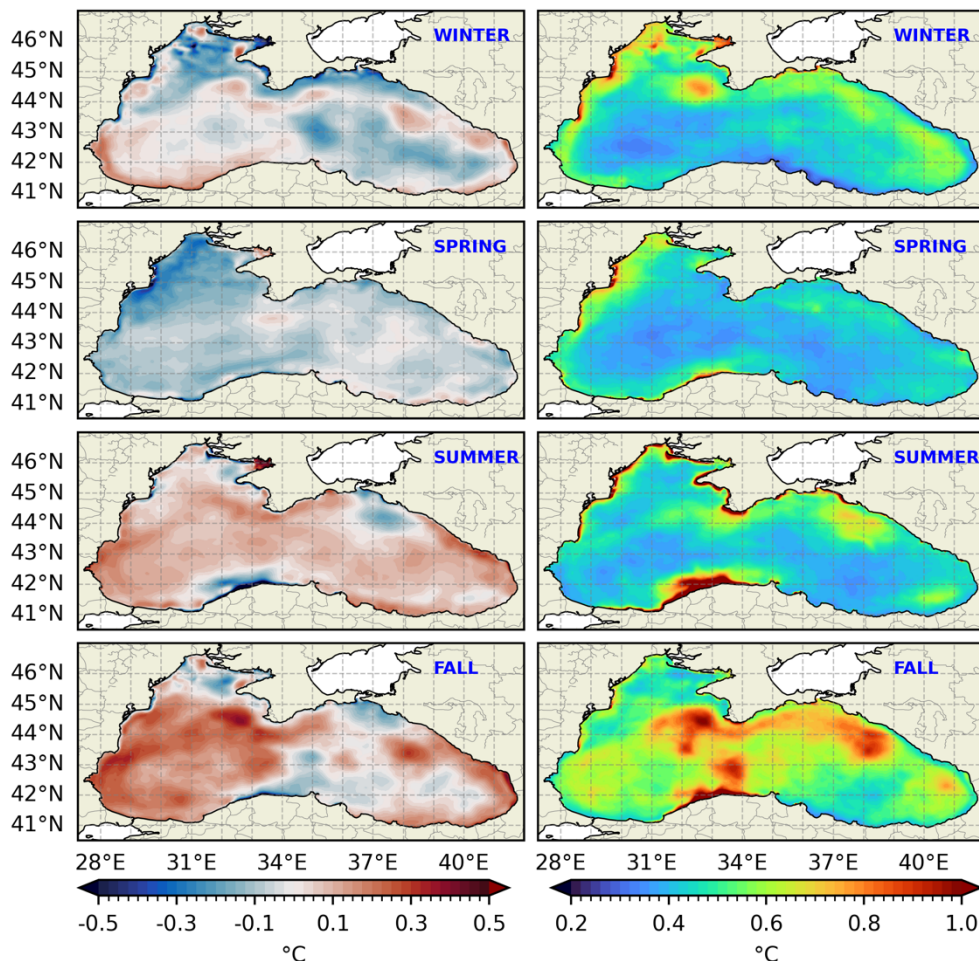
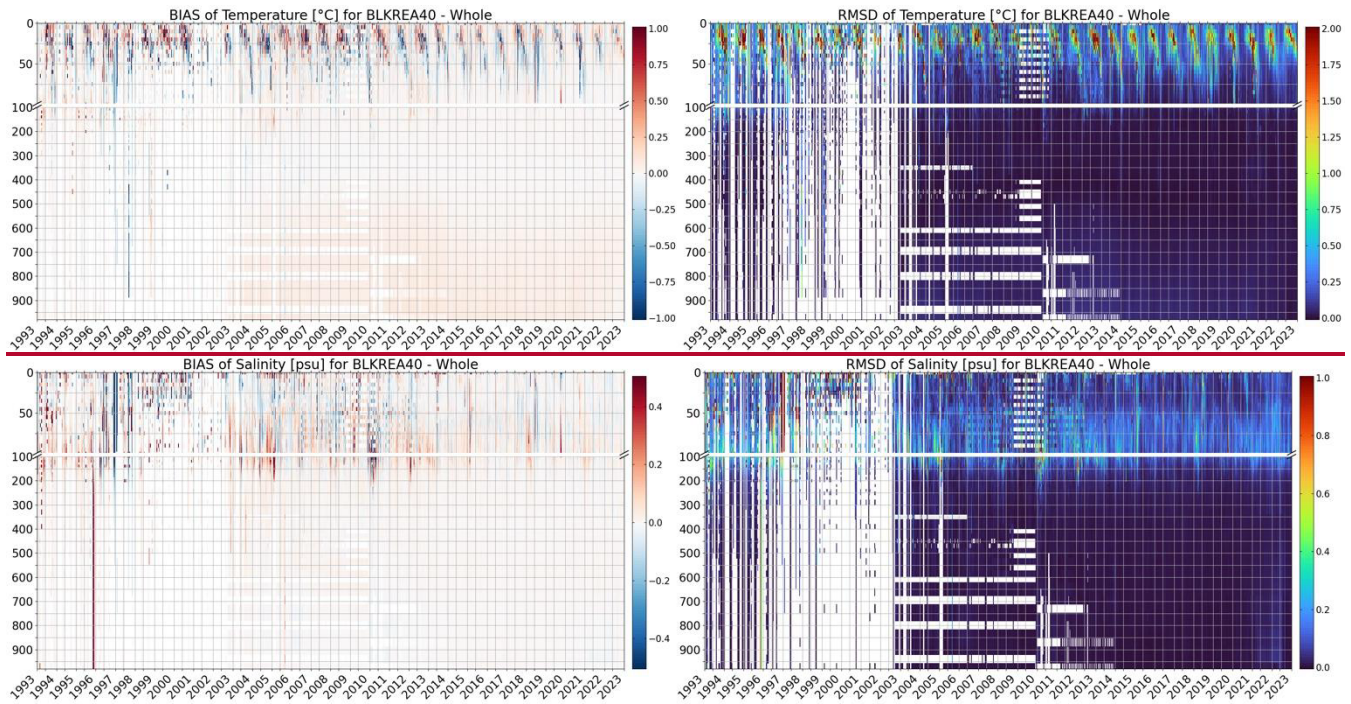


Figure 24: Seasonal maps of the mean bias (left) and RMSD (right) of the SST (°C) with respect to the satellite ESA-CCI product over the period between 1993 and 2022. From top to bottom: winter, spring, summer, and fall.

250

251 The Hovmöller diagram (time-depth) of RMSD for temperature computed as a lateral average, reveals a distinct seasonal cycle  
252 in the upper water column (Figure 32, top right), with lower errors in winter that increase during summer, exceeding 2°C in  
253 the upper 50 meters. This summer increase is associated with the model's misrepresentation of the seasonal thermocline, which  
254 is partially corrected through data assimilation. Below 100 m, errors remain low, staying below 0.25°C for almost the whole  
255 period. Before the Argo floats era (mid-to-late 2000s), the scarcity of in-situ data limited the effectiveness of data assimilation,  
256 compromising both the model correction and the validation process.



257

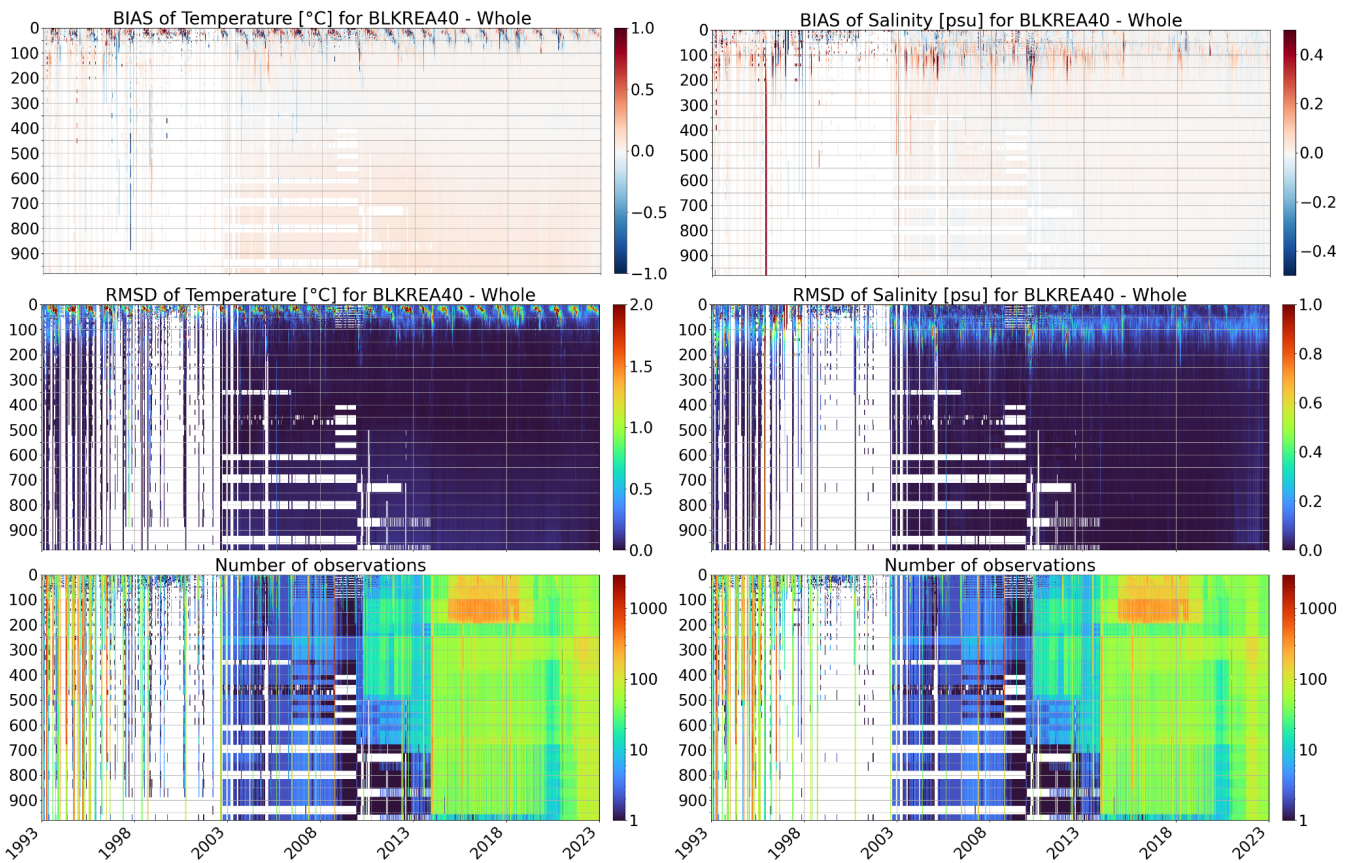


**Figure 32: Hovmöller (time–depth) diagrams of temperature (left) and salinity (right) in the Black Sea from 1 January 1993 to 31 December 2022. Rows show bias (top), RMSD (middle), and number of observations (bottom). Temperature is in °C and salinity in PSU. Hovmöller (time–depth) diagrams of bias (left) and root mean square difference (right) computed against observations of temperature in °C (top) and salinity in PSU (bottom) available in the Black Sea domain from 1 January 1993 to 31 December 2022.**

The Hovmöller diagram of temperature biases predominantly shows positive values, occasionally exceeding 1°C near the surface, with intermittent periods of negative biases (Figure 32, top-left). The most pronounced discrepancies are observed within the seasonal thermocline depths. There is a tendency for biases to shift from positive in upper layers to negative values at deeper layers, down to 100 m. This may be related to the misrepresentation of the vertical position of the seasonal thermocline in the BLK-REA results compared to observations over time.

Unlike temperature, the Hovmöller diagram of RMSD for salinity does not exhibit a clear seasonal cycle. Errors exceed 1 psu during short periods (Figure 3), particularly in the upper layers, where high uncertainties are likely derived from precipitation biases in ERA5, simplified river runoff forcing, and the internal freshwater budget computed via the model's bulk formulae. Unlike temperature, the Hovmöller diagram of RMSD for salinity does not exhibit a clear seasonal cycle (Figure 2, bottom right). Errors exceed 1 psu during short periods, particularly near the surface. Apart from these peak values, errors are relatively higher between 50 and 100 m. Within this layer, errors tend to decrease over time, reaching values below 0.25 psu

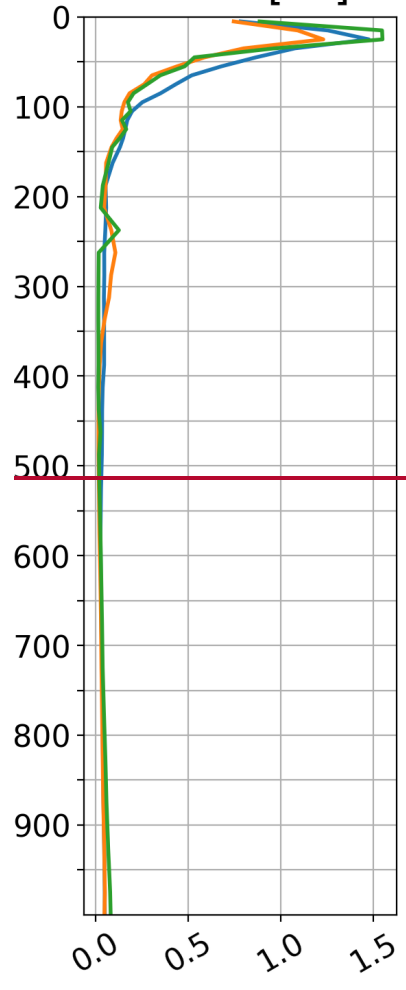
274 in the most recent years of validation. Once again, the scarcity of observations compromises the validation process before  
275 2004. Below 200 m, errors remain very low, with values consistently below 0.1 psu.

276 Salinity biases show a predominance of positive values (Figure [32, bottom-left](#)). The Hovmöller diagram reveals two main  
277 characteristics: BLK-REA diverges more from observations in the upper 200 m, with values alternating between positive and  
278 negative biases. Below 200 m, biases approach zero and remain predominantly positive. Since 2014, the values tend to be  
279 closer to zero, with biases showing a relative reduction in the upper 200 m.

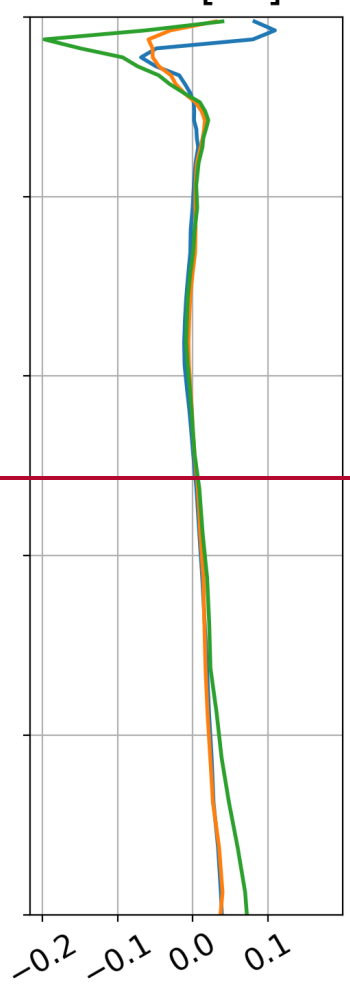
280 During the validation stage, the elevated T/S errors around 1996 (salinity) and 1998 (temperature) in the Hovmöller diagrams  
281 (Figure 3) may be linked to observations that were not assimilated but included in the quasi-independent validation. These  
282 peaks are likely due to reflect a combination of such observations, but also sparse coverage, and local model biases.

283 Figure [43](#) presents the temporal and spatial averaged RMSD and biases for temperature, comparing the reanalysis results with  
284 in-situ observations. For a better spatial analysis, we divide the Black Sea into three different regions: western, central, and  
285 eastern. The largest temperature errors occur in the upper layers and are primarily associated with the formation of the seasonal  
286 thermocline in summer, as previously shown in by the Hovmöller diagrams for temperatures shown by the Hovmöller diagram  
287 (Figure [32, top](#)). In this layer, RMSD reaches a maximum of approximately 1.5 °C in the western and eastern regions, and  
288 about 1.25 °C in the central region. In the upper water column, temperature biases are negative in the eastern and central  
289 regions. In the western region, the bias is positive from the surface down to 50 meters, reaching values of up to 0.1 °C, and  
290 becomes negative between 50 and 100 meters, aligning with the values observed in the central region. The largest errors are  
291 observed in the eastern region. Errors gradually decrease with depth, with RMSD reaching values lower than 0.25°C at 150  
292 m, biases becoming closer to zero.

RMSD [°C]



BIAS [°C]

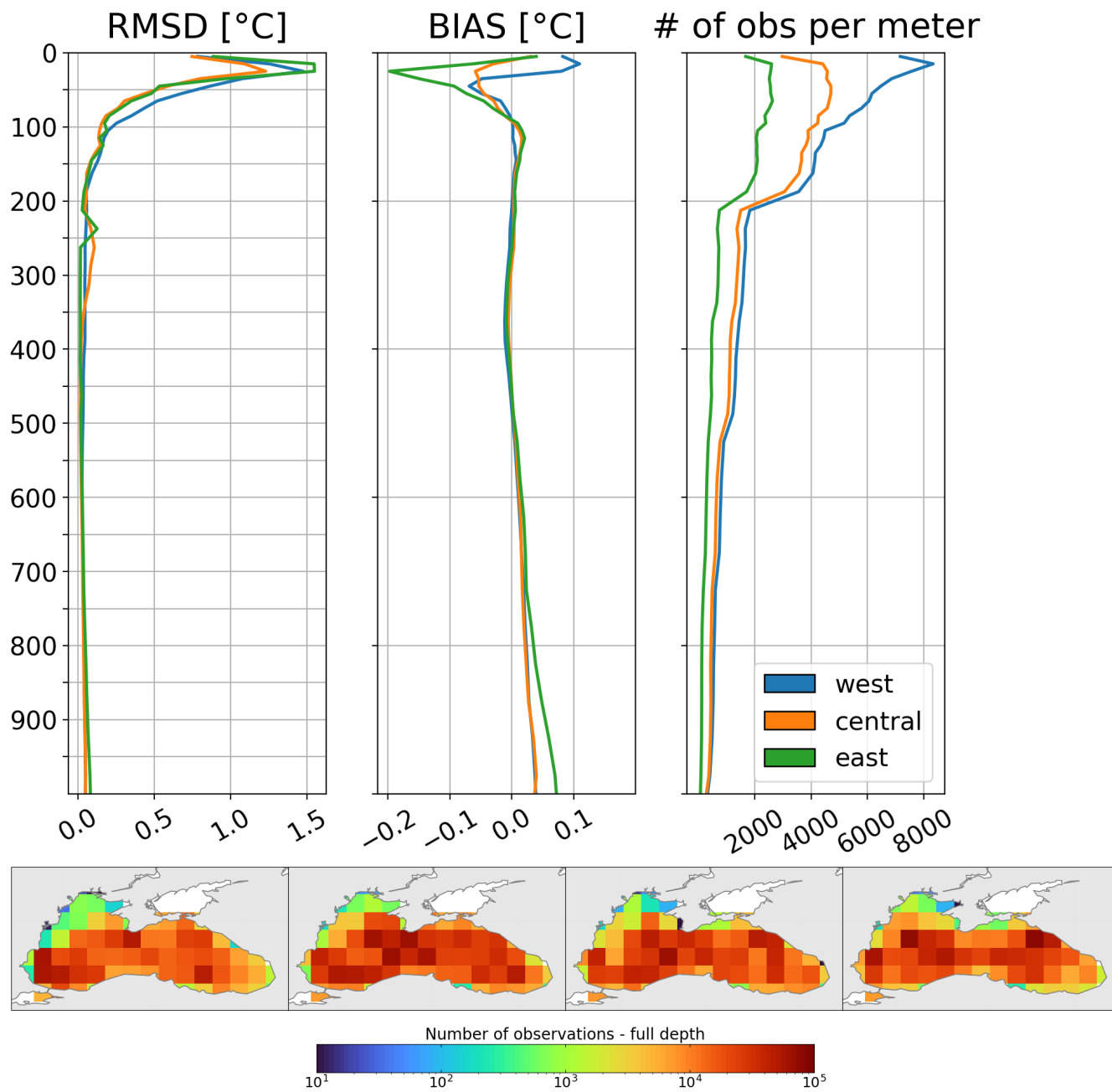


# of obs per meter



west  
central  
east

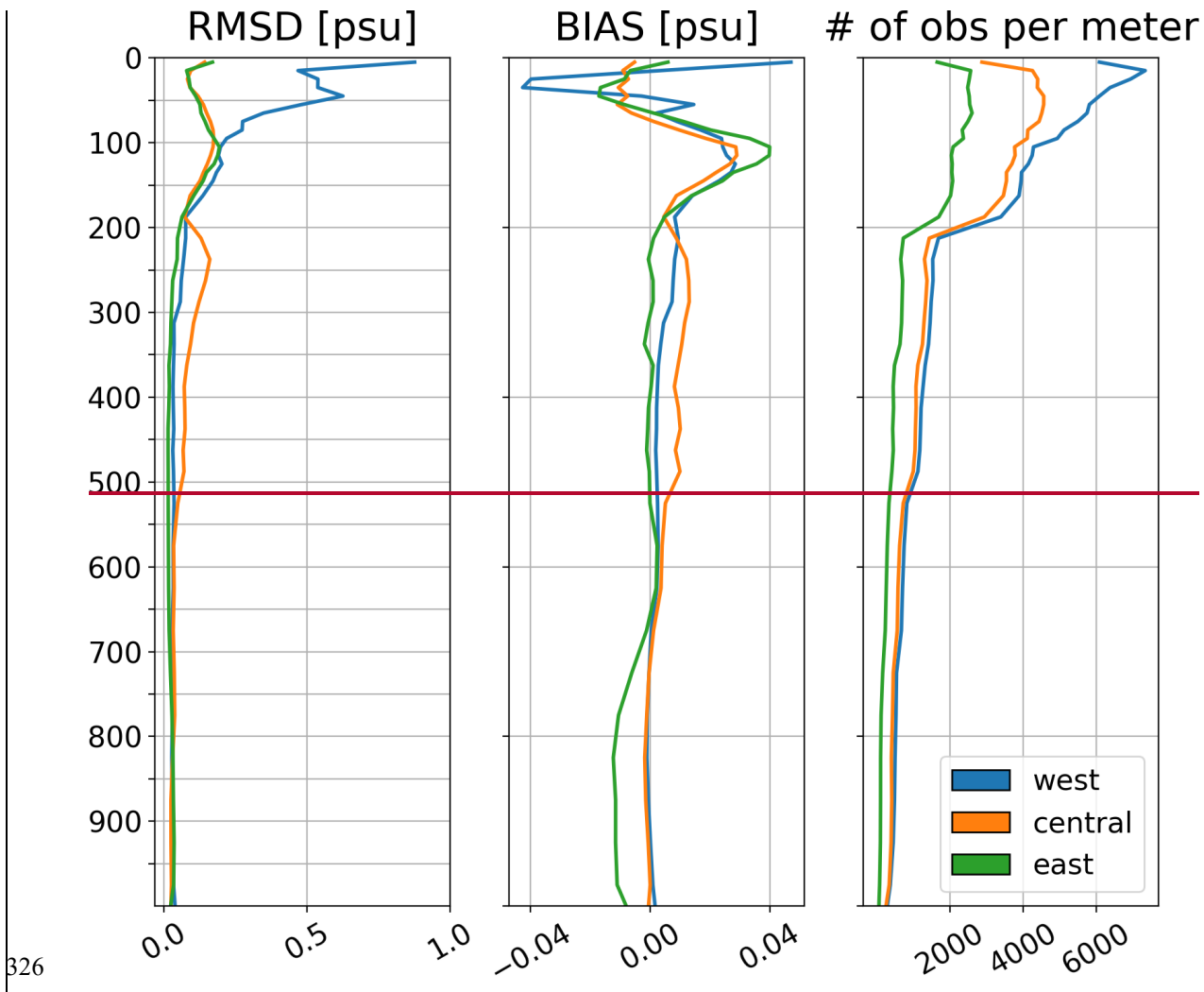
293



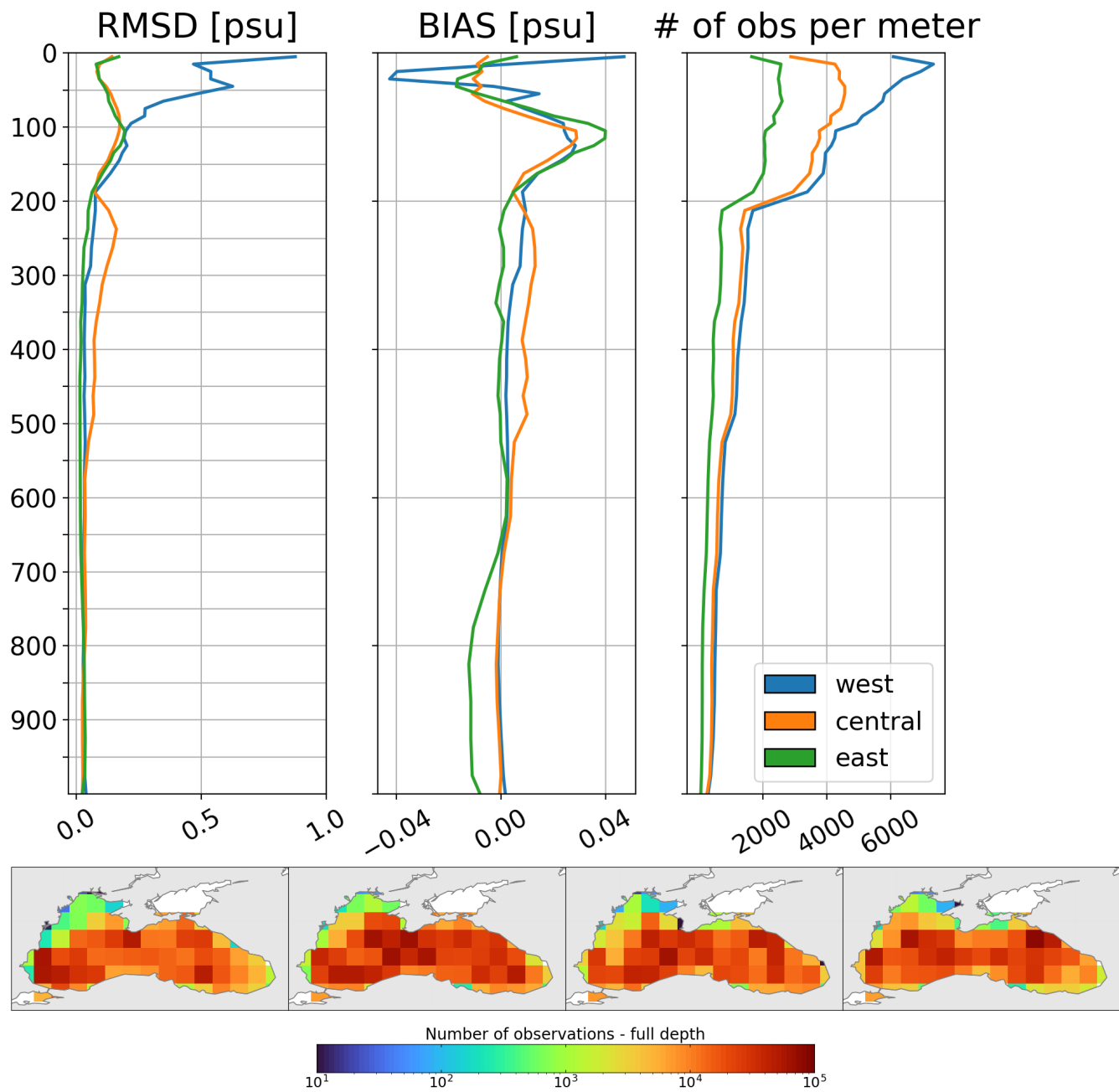
294  
 295 **Figure 43:** Vertical profiles of the RMSD (left panel), bias (middle panel) and number of observations (right panel) for temperature  
 296 (in °C), by comparing the reanalysis results against in-situ profilers in three areas (West, Central and East) of the Black Sea domain  
 297 from 1 January 1993 to 31 December 2022. Seasonal spatial maps at the bottom show the total number of temperature observations  
 298 throughout the entire water column, from left to right: winter, spring, summer, and fall.

300 The same analysis for salinity is shown in Figure 5. The western region exhibits the highest near-surface RMSD, with values  
301 reaching over 0.8 psu in the upper 100 m, despite high observational coverage. In contrast, RMSD values are lower in the  
302 central and eastern regions, remaining below 0.2 psu in the upper layers. These high elevated values in the western region are  
303 mainly due to limitations in freshwater inputs from major rivers: only the Danube uses monthly varying discharge, while other  
304 rivers follow climatologies without intra-annual variability, producing persistent local biases. Prescribed boundary conditions  
305 near the Bosphorus Strait improve the physical representation but also introduce uncertainties. Data assimilation can partially  
306 improve model representation under these circumstances by incorporating observations with strict quality control, but some  
307 errors can still persist. The same analysis is provided for salinity showing highest error and bias values in the upper 100 m in  
308 the western region, with an error exceeding 0.8 psu near the surface. RMSD values are lower in the central and eastern regions,  
309 where errors remain below 0.2 psu throughout the water column (Figure 4). Salinity biases show regional differences. In the  
310 western region, positive biases are pronounced near the surface, rapidly transitioning to negative values and reaching about –  
311 0.04 psu between 25 and 50 m. In contrast, biases in the surface layers of the central and eastern regions remain closer to zero  
312 but increase in the subsurface starting at 50 m, following the pattern observed in the western region. Bias values are in general  
313 small, and in particular in the western region, biases are high and positive near the surface, rapidly transitioning to negative  
314 values, reaching –0.04 psu between 25 and 50 meters. In contrast, salinity biases in the surface layers of the central and eastern  
315 regions are close to zero, but they increase in the subsurface starting at 50 meters, following the values observed in the western  
316 region. At a depth of around 100 meters, all regions exhibit relatively high salinity biases, with the eastern region showing the  
317 highest values, reaching up to 0.04 psu. In general, salinity biases decrease beneath 100 meters and approach zero at depths  
318 greater than 200 meters.

319 In the Eastern region, a slight increase in temperature and salinity biases occurs below 700 m (Figures 4 and 5). This pattern  
320 likely arises from sparse deep-layer observations prior to 2003 (as shown in the Hovmöller diagrams, Figure 3), limitations in  
321 model initialization, and unresolved physical processes within the model. The introduction of Argo profiling floats from 2003  
322 increased deep data coverage, revealing biases that were previously undetected and never corrected; below 700 m, LSBC  
323 toward WOA2018 climatology is not sufficient to constrain the model. In addition, some observations excluded from  
324 assimilation were still included in validation, further contributing to the apparent increase in errors. Even with strict quality  
325 control, some measurement errors or inconsistencies may have persisted.



326



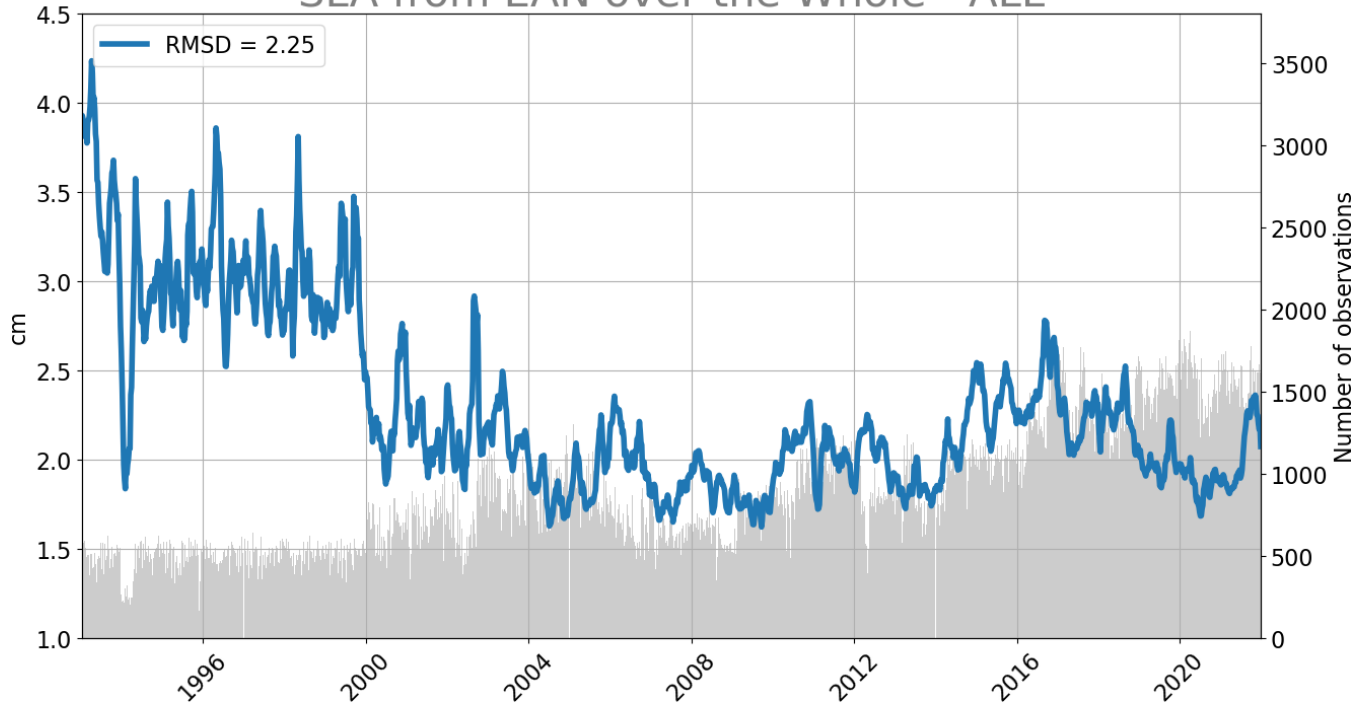
327

328 **Figure 54:** Vertical profiles of the RMSD (left panel), bias (middle panel) and number of observations (right panel) for salinity (psu),  
 329 by comparing the reanalysis results against in-situ profilers in three areas (West, Central and East) of the Black Sea domain from 1  
 330 January 1993 to 31 December 2022. Seasonal spatial maps at the bottom show the total number of salinity observations throughout  
 331 the entire water column, from left to right: winter, spring, summer, and fall.

332

333 The time series of spatially averaged SLA RMSD (Figure 6) shows strong skill after 2000, with errors around 0.02 m, below  
334 the instrumental error of 0.04 m used in assimilation. This improvement reflects the increased availability of satellite altimetry,  
335 while in situ T/S profiles remained scarce, making leaving SLA as the main constraint on the model. Instead, the slight RMSD  
336 increase around 2016 coincides with the larger availability of Argo profiles. Their assimilation, together with SLA, may have  
337 slightly degraded SLA skill due to the multivariate nature of the system. Nevertheless, the RMSD remains well within  
338 acceptable limits, and these points are intended to provide an overview of SLA performance rather than a detailed attribution  
339 of small temporal fluctuations.~~The time series of spatially averaged SLA RMSD (Figure 5) indicates that, after the year 2000,~~  
340 ~~the BLK-REA demonstrates strong performance with high skill and errors typically around 0.02 m. This is well within~~  
341 ~~acceptable limits, as it remains below the observation error for SLA in data assimilation, which is 0.04 m.~~ It is to be noted that  
342 the evaluation is performed in areas deeper than 1000 m, considered as the level of no motion when assimilating SLA data  
343 through a dynamic height operator. Spatial maps of the sea level anomaly RMSD reveal the highest values, ranging from 2.5  
344 to 4 cm, with occasional peaks exceeding 4 cm, predominantly along the basin's periphery (Figure 76). These elevated  
345 deviations are closely linked to the Rim Current and its inherent mesoscale variability. In contrast, SLA RMSD values in the  
346 central basin are generally lower, around 2 cm. Notably, areas with large RMSD values align with regions of strong eddy  
347 kinetic energy (EKE), which we use to assess mesoscale activity (Figure 87). This pattern is particularly evident along the  
348 Anatolian, Caucasian, and Crimean coasts, where well-known mesoscale characteristics are present (Koroatev et al., 2003).  
349 SLA errors show slight variations across seasons, with particular attention given to high values along the Caucasian coast.  
350 These values extend further offshore in winter. Additionally, higher SLA errors occupy a larger area around the Batumi eddy  
351 region during fall. Error values are relatively high along the Crimean coast, particularly in the western region, where the  
352 persistent influence of the Sevastopol eddy contributes to elevated mesoscale variability. However, these errors tend to  
353 decrease during summer. Kubryakov and Stanichny (2015) reported that the total number of detected eddies exhibits local  
354 maxima in both the Sevastopol and Batumi eddy regions, reflecting the dynamic nature of coastal circulation in these areas.  
355 These complex dynamics may not be adequately resolved by the model, potentially contributing to elevated SLA errors in  
356 these areas.

## SLA from EAN over the Whole - ALL

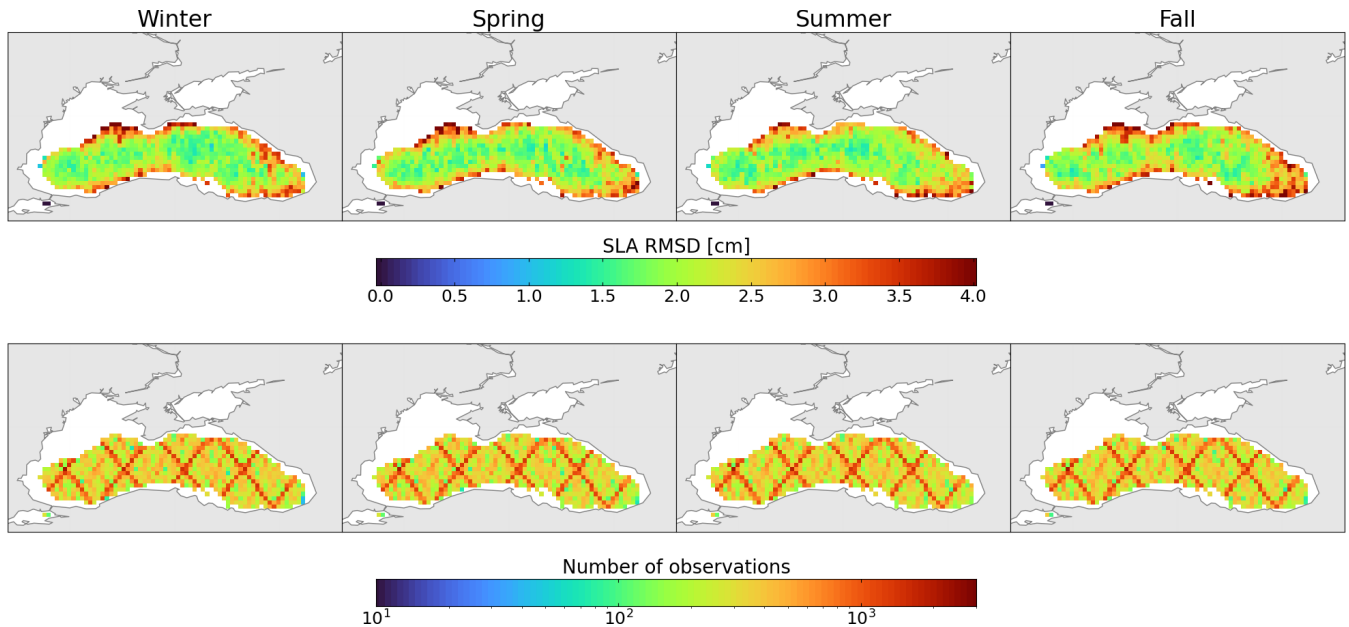


357

358

359

**Figure 65:** Time evolution of basin-averaged SLA RMSD, comparing BLK-REA with satellite along-track SLA data, with a 7-day moving average applied to smooth short-term variability.



360

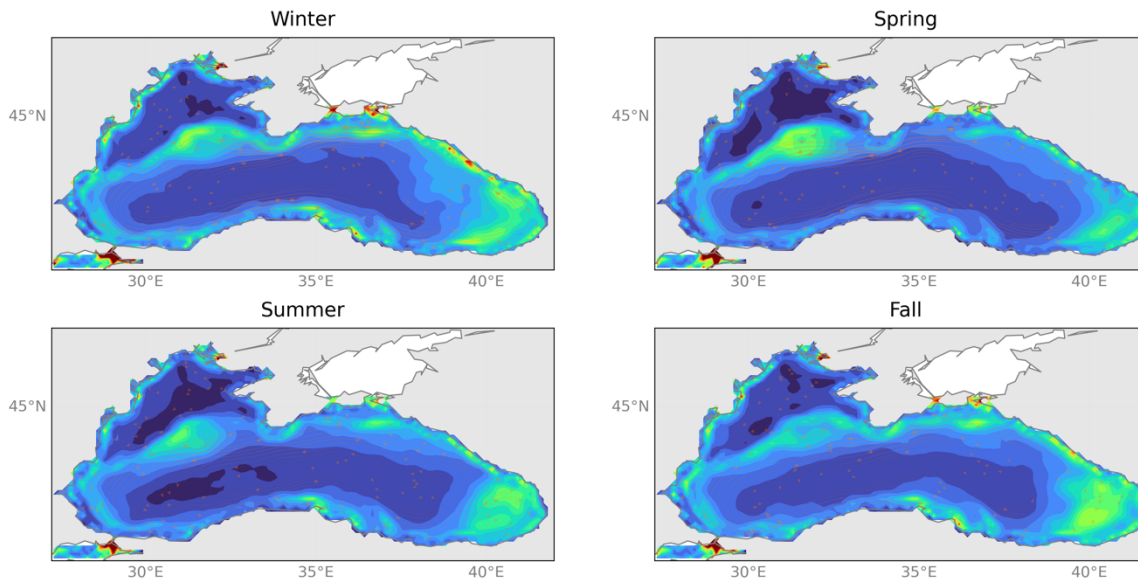
361

362

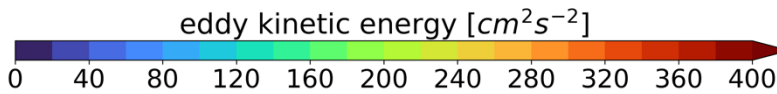
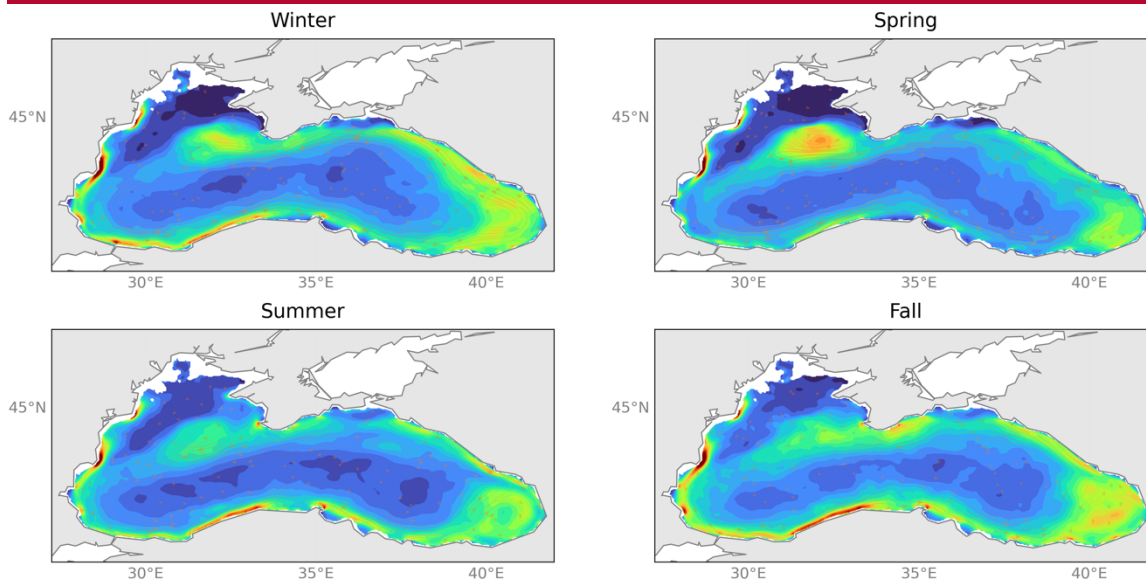
**Figure 76:** Seasonal maps of the mean RMSD (top) of the SLA (cm) with respect to the satellite along-track SLA product over the period between 1993 and 2022. Bottom maps indicate the number of observations for each season.

363 This interpretation is further supported by EKE maps (Figure 8), which consistently show high energy levels in these regions,  
364 indicating intense mesoscale activity that aligns with the SLA discrepancies viewed in Figure 7. EKE maps show elevated  
365 values along the Rim Current, particularly along the Caucasian coast. To ensure a clean comparison with altimetry-derived  
366 estimates, BLK-REA EKE was computed from the geostrophic component only, using SSH from the model. BLK-REA EKE  
367 values generally exceed those derived from altimetry, especially in the Batumi and Sevastopol eddies, where peak values reach  
368 about  $300 \text{ cm}^2 \text{ s}^{-2}$  in fall and spring, respectively, compared to altimetry-based estimates of around  $220 \text{ cm}^2 \text{ s}^{-2}$ . This difference  
369 likely reflects multiple factors, including the spatial smoothing inherent to the  $0.25^\circ$  Level-4 altimetry product, the reduced  
370 capability of altimetry to capture smaller-scale variability due to mapping and interpolation procedures, and possible over-  
371 energetic behaviour of the model arising from its higher resolution, physical parameterizations, and potentially insufficient  
372 dissipation of mesoscale energy.~~This interpretation is further supported by EKE maps (Figure 7), which consistently show~~  
373 ~~high energy levels in these regions, indicating intense mesoscale activity that aligns with the SLA discrepancies viewed in~~  
374 ~~Figure 6. EKE maps show elevated values along the Rim Current, particularly along the Caucasian coast. EKE values from~~  
375 ~~the BLK-REA generally exceed those derived from altimetry, likely due to the lower resolution of the Level 4 altimetric~~  
376 ~~product, which has a spatial resolution of 0.25 degrees. In fact, BLK-REA EKE results surpass the altimetry-derived estimates,~~  
377 ~~showing peak values of approximately  $300 \text{ cm}^2 \text{ s}^{-2}$  in the Batumi and Sevastopol eddies during fall and spring, respectively,~~  
378 ~~while altimetry-based EKE in the same regions and seasons reaches around  $220 \text{ cm}^2 \text{ s}^{-2}$ .~~

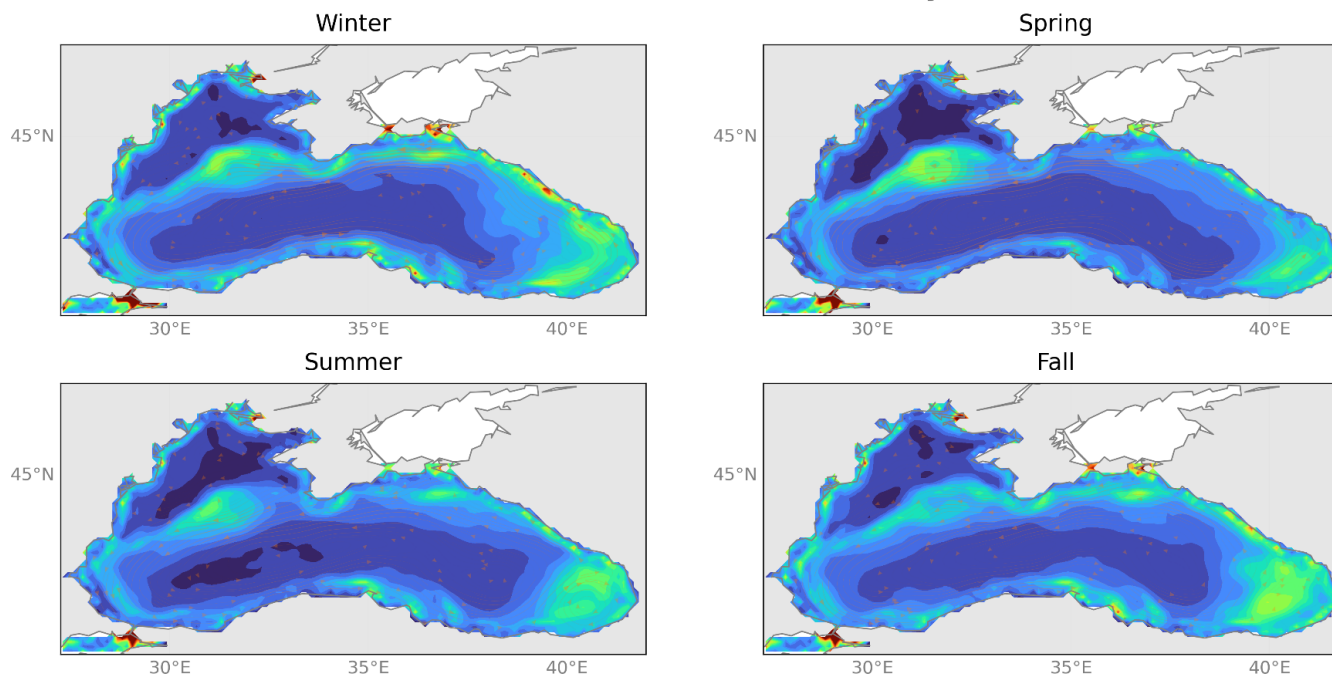
### seasonal EKE from altimetry for layer: surface



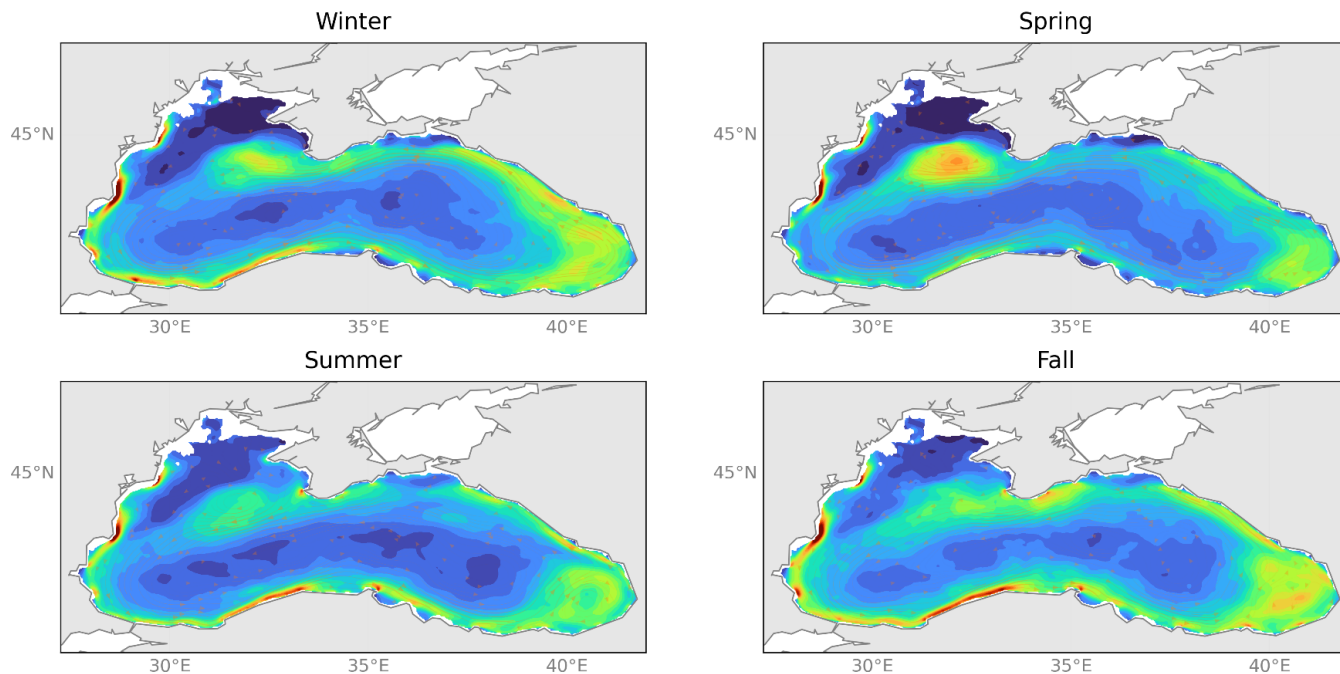
### BLKREA40 seasonal EKE for layer: surface



# seasonal EKE from altimetry



# BLKREA40 seasonal EKE



eddy kinetic energy [ $cm^2s^{-2}$ ]



381

382 **Figure 87:** Seasonal maps of eddy kinetic energy (EKE) ( $\text{cm}^2 \text{s}^{-2}$ ) from satellite SLA L4-product and BLK-REA over the period  
383 between 1993 and 2022, based on the surface geostrophic velocity component.

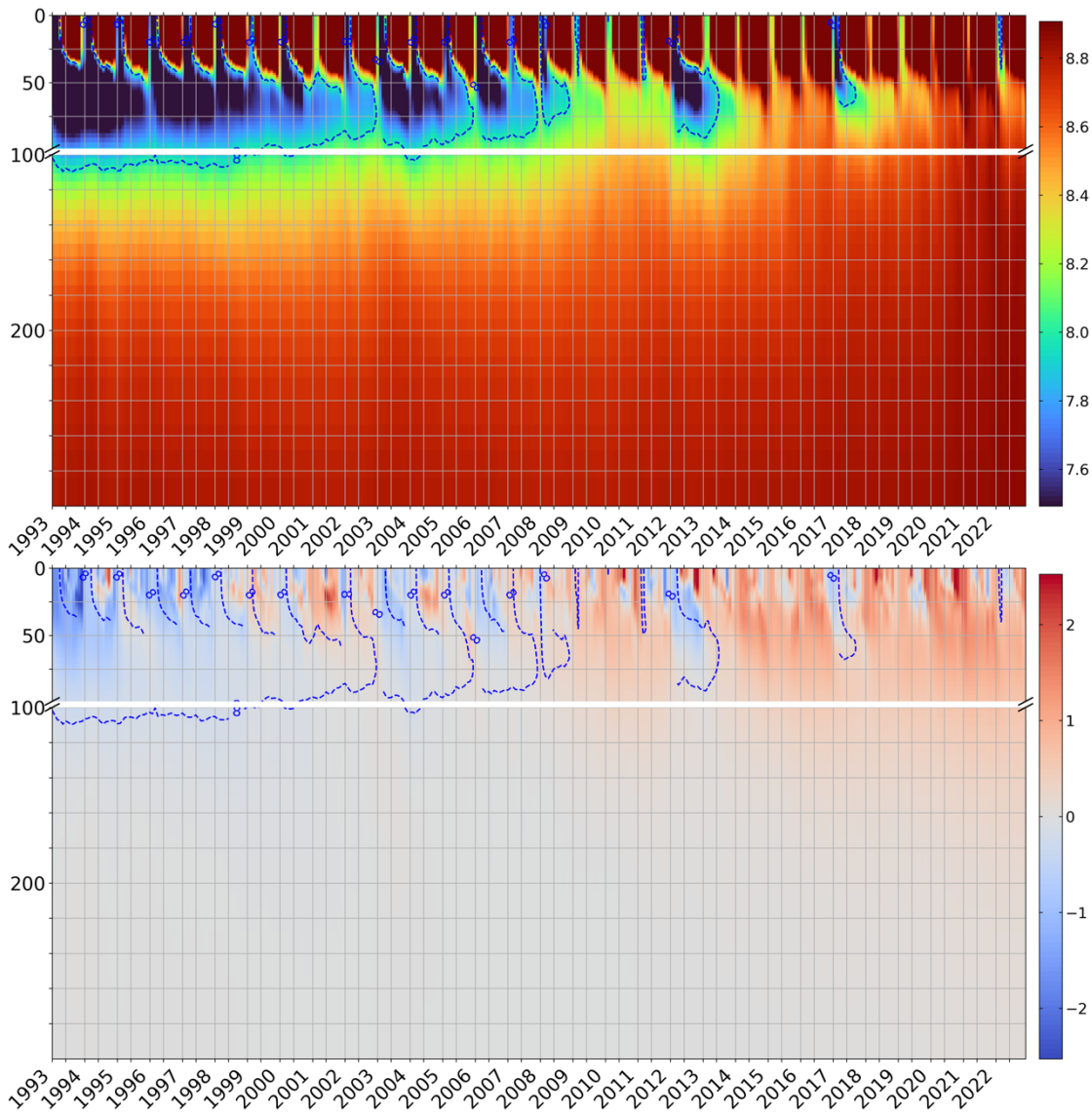
384

## 385 **3.2 Ocean monitoring indicators**

386 We present a set of OMIs computed from the BLK-REA: ocean heat content, Rim Current interannual variability, and  
387 meridional overturning circulation. These indicators provide valuable insights into key aspects of Black Sea dynamics.

### 388 **3.2.1 Ocean heat content**

389 Figure 98 illustrates the time evolution of basin-averaged temperature, with the 8 °C isotherm selected to track the Black Sea  
390 CIL over time. The formation of the CIL is mainly associated with water cooling during the winter season, and its presence is  
391 consistently observed until 2008. From 1993 to 2008, the CIL extends from the surface to approximately 100 meters in depth.  
392 After 2008, this pattern exhibits a significant shift, as temperatures rise, leading to the frequent disappearance of the CIL.  
393 Nevertheless, instances of CIL formation are also observed in 2012, with a reduced extent in 2017, consistent with Argo float  
394 measurements (Stanev et al., 2019). More recently, a very weak CIL formed in March 2022, as documented by Çokacar et al.  
395 (2024), who attributed this event to intense cold-air masses that caused severe weather conditions across southern Europe,  
396 including the Black Sea, and influenced CIL formation.



397  
 398 **Figure 98:** Hovmöller (time-depth) diagrams of monthly basin-averaged temperature in °C (top) and anomaly of temperature in °C  
 399 (bottom). The monthly anomaly estimates considered the climatological period 1993–2014 of each corresponding month. The blue  
 400 dashed line indicates the mean position of the 8°C isotherm (top).

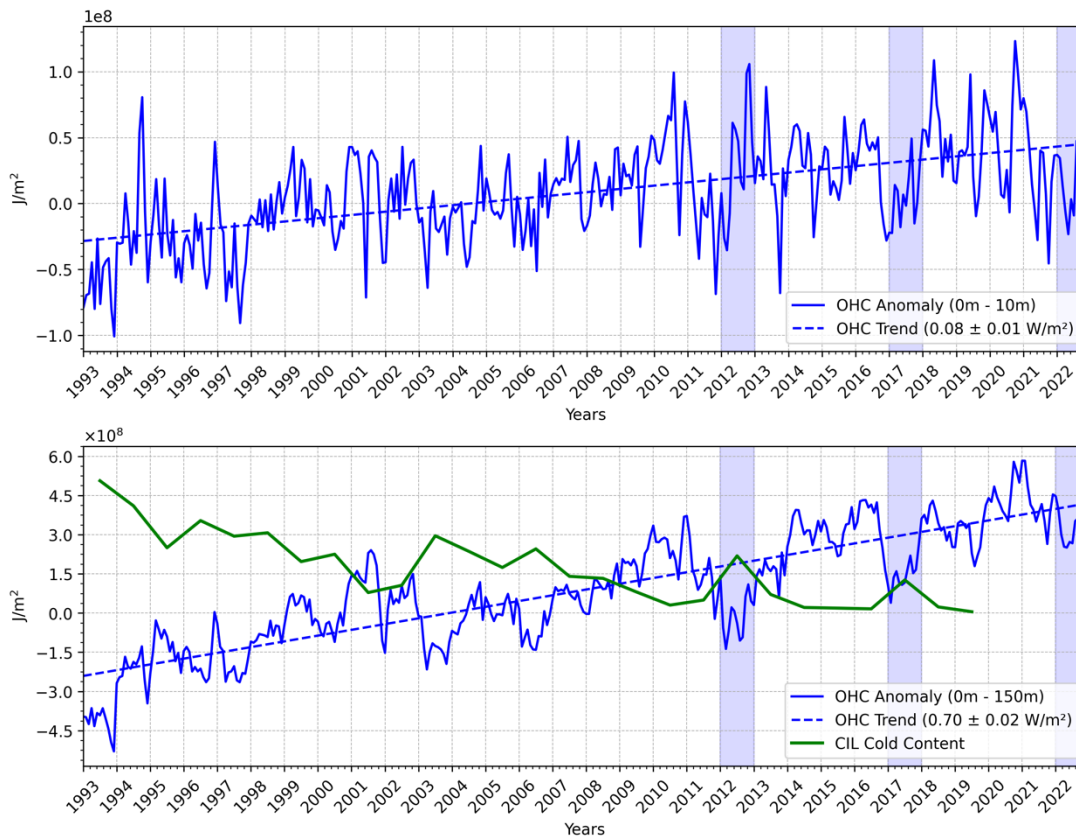
401 The warming signal is evident in the Hovmöller diagram of temperature anomalies, which shows a predominance of positive  
 402 values starting in 2009. Occasionally, positive values are interrupted by negative anomalies in the upper layers, as seen in years  
 403 with the presence of the CIL: 2012, 2017, and 2022.

404 The analysis of ocean heat content in the Black Sea follows the formulation outlined by Lima et al. (2020), as described by the  
 405 equation below:

406 
$$OHC = \int_{z_1}^{z_2} \rho_0 c_p (T_m - T_{clim}) dz \quad (3)$$

407 with  $\rho_0$  equal to  $1020 \text{ kg m}^{-3}$  and  $c_p$  equal to  $3980 \text{ J kg}^{-1}\text{C}^{-1}$  are, respectively, the density and specific heat capacity; and  $dz$   
408 indicates a certain ocean layer limited by the depths  $z_1$  and  $z_2$ ;  $T_m$  corresponds to the monthly averaged temperature and  $T_{clim}$   
409 is the climatological temperature of the corresponding month. In this study, OHC is calculated as the deviation from the  
410 reference period of 1993–2014.

411 The OHC in both the 0-10 m and 0-100 m layers shows an overall warming trend, with values of  $0.08 \text{ W m}^{-2}$  and  $0.59 \text{ W m}^{-2}$ ,  
412 respectively (Figure 109). Table 1 shows OHC trends within other layers to compare the values with those reported by Lima  
413 et al. (2021), who analyzed OHC trends using the previous Black Sea reanalysis (Lima et al., 2021) during the period 1993–  
414 2018. In general, the newest BLK-REA shows lower OHC trends. In the 0-10 m layer, the OHC curve shows several positive  
415 peaks around  $1 \times 10^8 \text{ J m}^{-2}$  in 2010, 2012, 2018, and 2020. In contrast, negative peaks are observed in 1993, 1997, and 2001.  
416 An interesting observation is that although the CIL is present in 2012, there are positive anomalies in the upper layers that  
417 year. This suggests that colder waters from the upper layers, which subducted in 2011, may have reached the CIL levels in  
418 2012. These features are visible in the Hovmöller diagrams of basin-averaged temperature anomalies (Figure 98). The CIL  
419 signal is clearly present in the 0-100 m layer in 2012. Additionally, the OHC shows a clear agreement with the CIL cold content  
420 observed in the data, which was estimated by Capet et al. (2020) using temperature observations from various platforms.  
421 Specifically, years of higher heat content correspond to a reduction in CIL cold content, while years of lower heat content  
422 coincide with an increase in CIL cold content. In more recent years, the CIL cold content values are nearly zero, except for  
423 2012 and 2017, when the values exceeded  $1.5 \times 10^8 \text{ J m}^{-2}$  in 2012 and were slightly below this threshold in 2017; see the green  
424 curve in Figure 109. Correspondingly, both years show a decrease in OHC, reinforcing the relationship between CIL cold  
425 content and heat content variability.



426

427

428

429

430

431

**Figure 109:** Monthly basin-averaged of the ocean heat content anomalies (in  $\text{J m}^{-2}$ ) estimated for the BLK-REA in 0-10 m (top) and 0-100 m (bottom). The monthly ocean heat content anomalies are defined as the deviation from the climatological ocean heat content mean (1993–2014) of each corresponding month. Mean trend values are also reported for each layer (bottom right corner). In 0-100 m (bottom), the green curve corresponds to the CIL cold content from Capet et al. (2020). The blue shades highlight the recent years when the CIL is present: 2012, 2017 and 2022.

432

433

434

435

**Table 1:** Trends estimations together with the 95% confidence interval (in brackets) for the ocean heat content anomaly ( $\text{W m}^{-2}$ ) from BLK-REA for the periods 1993–2022 and 1993–2018, and from the previous Black Sea reanalysis (Lima et al., 2021) for the period 1993–2018.

	1993-2022	1993-2018	
	BLK-REA	BLK-REA	Lima et al. (2021)
0-10 m	0.08 (0.01)	0.09 (0.01)	0.11 (0.01)
0-50 m	0.35 (0.02)	0.37 (0.02)	0.45 (0.04)
0-200 m	0.74 (0.02)	0.72 (0.03)	0.81 (0.05)
0-1000 m	0.84 (0.02)	0.83 (0.03)	0.83 (0.04)

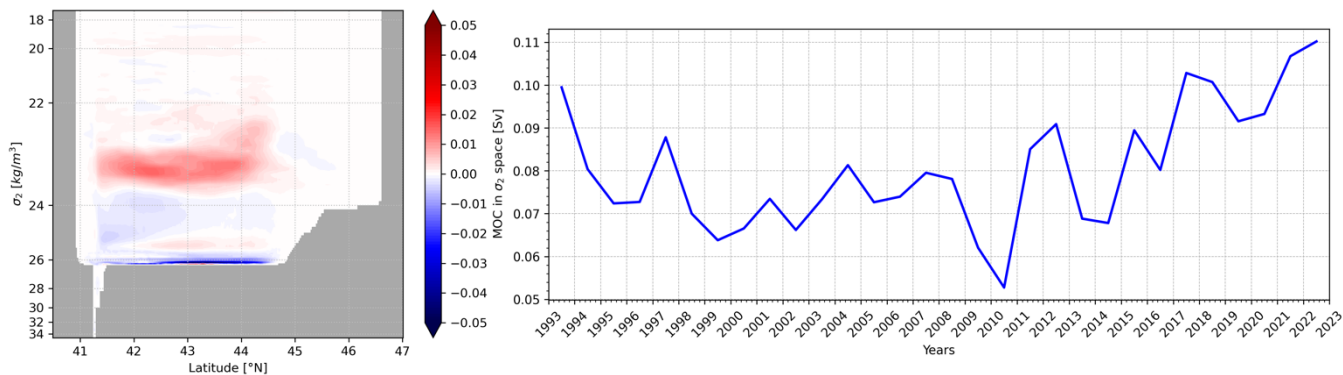
436  
437

### 438 3.2.2 The Black Sea overturning circulation

439 We follow the methodology of Ilicak et al. (2022), computing the meridional overturning circulation (MOC) in density space  
440 to better represent water mass transport in the Black Sea. We divide the water mass structure of the Black Sea in 50 different  
441  $\sigma_2$  ( $\sigma_2$ ; potential density anomaly with [ $\text{kg m}^{-3}$ ] respect to a reference pressure of 2000 dbar) density bins and compute  
442 the MOC using the formula:

$$443 \psi^*(y, \bar{\sigma}) = -\frac{1}{T} \int_{t_0}^{t_1} \int_{x_{B1}}^{x_{B2}} \int_{-H}^0 H[\bar{\sigma} - \sigma(x, y, z, t)] \times v(x, y, z, t) dz dx dt \quad (4)$$

444 where  $H$  is the Heaviside function and  $v$  is the meridional velocity. We used 100  $\sigma_2$  density bins to remap the mass flux fields.  
445 A very narrow cell with positive values (clockwise circulation) of approximately 0.03–0.04 Sv is observed just below 26  $\text{kg m}^{-3}$   
446  $\text{m}^{-3}$  around 43°N (Figure 110). However, at densities higher than 26  $\text{kg m}^{-3}$ , the MOC structure predominantly exhibits  
447 negative values (indicative of anticlockwise circulation), exceeding -0.03 Sv. At a density of approximately 25.5  $\text{kg m}^{-3}$ , the  
448 MOC forms a dipole pattern, with slightly positive values between 42°N and 44.5°N and negative values south of 42°N. Above  
449 this, the circulation remains anticlockwise until approximately 23.75  $\text{kg m}^{-3}$ , where a clockwise pattern re-emerges between  
450 23.75  $\text{kg m}^{-3}$  and 22  $\text{kg m}^{-3}$ , with positive transport exceeding 0.02 Sv. Nonetheless, within this layer, localized negative  
451 values are observed, particularly around 45°N. In general, below 23.75  $\text{kg m}^{-3}$ , there is a predominance of anticlockwise  
452 circulation, especially in the southern part of the basin, likely associated with the inflow of Mediterranean Water into the Black  
453 Sea. Above this isopycnal, positive values indicate a clockwise circulation, which is linked to the formation of the CIL. These  
454 findings are consistent with the results of Ilicak et al. (2022).



455

456 **Figure 110: Time-mean overturning transport in density space (left); Time evolution of the maximum BLK-MOC in density space**  
457 **between 22.45 and 23.85  $\text{kg m}^{-3}$  (right).**

458 Next, we identify the maximum MOC in density space for the Black Sea between 22.45 and 23.85  $\text{kg m}^{-3}$ , corresponding to  
459 depths of approximately 25 to 80 m (Ilicak et al., 2022). The MOC declined from 0.1 Sv in 1993 to a minimum of nearly 0.01  
460 Sv in 2010. After 2010, the MOC exhibited alternating periods of increase and decrease, but with an overall upward trend,

461 reaching its highest values of almost 0.12 Sv in 2022. Stanev et al. (2019) reported that the Black Sea MOC has weakened  
462 over the past 30 years, possibly due to anthropogenic global warming. In recent years, the CIL has nearly disappeared, as  
463 shown by observational data and reanalysis results (Stanev et al., 2019; Lima et al., 2021; Capet et al., 2020), as also discussed  
464 in the OHC section (Figures 98 and 109). Ilicak et al. (2022) associated the decline in MOC with the loss of CIL cold content  
465 between 1993 and 2010. However, since 2010, the MOC has started to increase, while the CIL is only present in 2012 and  
466 remains very weak in 2017 and 2022. Different water mass transformations could be the potential mechanisms behind an  
467 increase in the MOC. Specifically, an increase in salinity could compensate for the decrease in the formation of cold, dense  
468 water, which would otherwise weaken the circulation. Reanalysis model results show that there is an upward trend of SSS in  
469 the Black Sea. In addition, running multiple cycles of decadal reanalysis simulations is likely necessary to achieve a more  
470 accurate spin-up of the deep ocean. However, to investigate the detailed dynamics of the meridional overturning circulation  
471 (MOC) in the Black Sea, further research is required. This should involve using multi-cycle reanalysis model simulations  
472 combined with passive tracers, such as ideal age, to better understand the circulation patterns and timescales.

473  
474 ~~This suggests that factors other than the CIL may be influencing the Black Sea MOC and should be investigated in detail.~~

### 475 3.2.3 The Rim Current interannual variability

476 The Rim Current is the dominant cyclonic gyre that defines the general circulation of the Black Sea. The Black Sea Rim  
477 Current Intensity Index (BSRCI) measures the strength of this current in a given year relative to the multi-year average. It is  
478 based on the average surface current velocity in the Rim area confined by the isobaths of 200 and 1800 m. Two sections are  
479 chosen as representative for the Rim current: a northern section between 33°E–39°E, and a southern section between 31.5°E–  
480 35°E. For each section, the BSRCI is defined as:

$$481 \text{BSRCI} = \frac{\bar{v}_{ann} - \bar{v}_{cl}}{\bar{v}_{cl}} \quad (5)$$

482 with  $\bar{v}_{ann}$  the annual average surface current speed in the respective area and  $\bar{v}_{cl}$  the long-term average over the period 1993-  
483 2022. In this way, the index is close to zero when the annual mean state is near normal, while positive values indicate a stronger  
484 Rim Current, and negative values represent a weaker one (Peneva et al., 2021; von Schuckmann et al., 2021). The BSRCI OMI  
485 provides the intensity of the Rim Current in both the Northern and Southern Black Sea. In this study, we present updated  
486 results based on the latest data from the Black Sea reanalysis. The values are predominantly negative before 2010, with a  
487 notable negative peak below -0.2 in 1997 (Figure 12+). After 2010, the values alternate between negative and positive, with  
488 positive peaks observed in 2014, 2017, 2020, and 2022. The BSRCI peak in 2014 exceeds 0.15 and reaches a maximum of  
489 over 0.25 in the southern branch. The intensity in both branches generally coincides, though the southern branch typically  
490 exhibits higher values. Peneva et al. (2021) also identified a peak in 2014 using results from the previous Black Sea reanalysis.  
491 The current analysis reveals a trend of +2.9% per decade, which is a value compatible with Peneva et al. (2021) as well.

We also present the wind stress curl (Figure 124), diagnosed using the NEMO bulk formulation at the model's native resolution, based on ERA5 wind data. As previously suggested by Stanev et al. (2000) and further examined by Peneva et al. (2021), the wind stress curl plays a key role in modulating the Rim Current. Our results support this relationship, showing strong agreement between years of enhanced mean wind stress curl and increased intensity of the Black Sea Rim Current Index (BSRCI), particularly in 2014 and 2018. This correspondence is especially evident in the southern section of the basin.

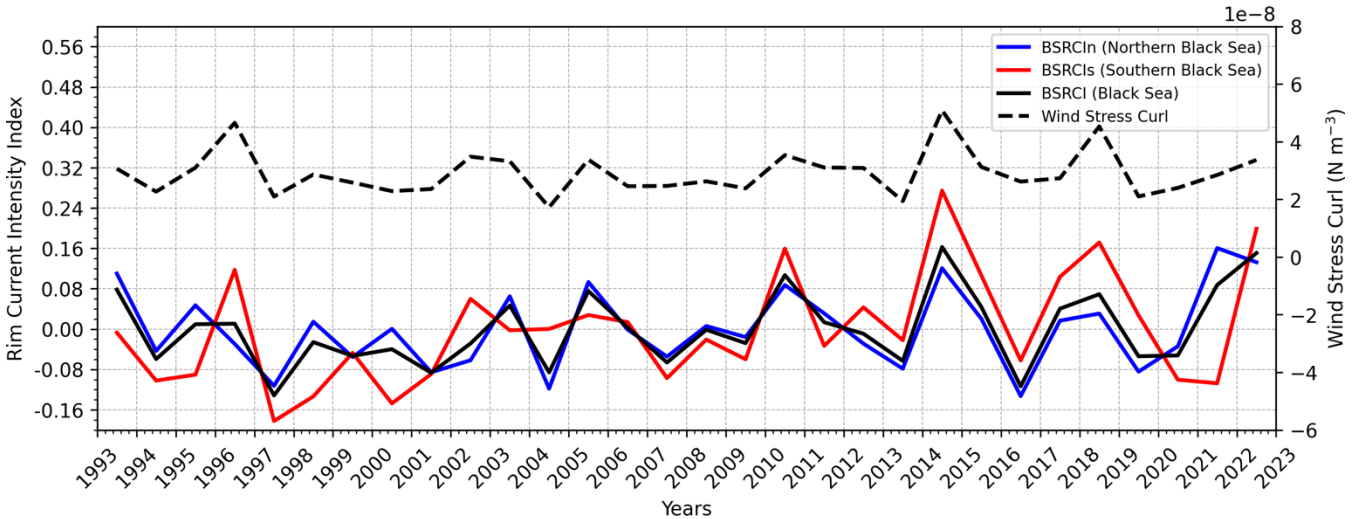


**Figure 124:** Time series of the Black Sea Rim Current Index (BSRCI; black) at the north section (BSRCIn; blue), south section (BSRCIs; red), the average (BSRCI) and its tendency for the period 1993-2020. The black dashed curve represents the annual mean wind stress curl ( $\text{N m}^{-3}$ ) averaged for the Black Sea based on the ERA5 reanalysis.

#### 4 Discussion and Outlook

The new BLK-REA features a higher model resolution, providing a more consistent and accurate representation of Black Sea physics. The updated configurations include the use of LOBCs, allowing improved water exchange through the Bosphorus Strait. This enabled further refinements in the freshwater balance to be implemented, such as incorporating hourly precipitation data and monthly runoff for the Danube River. These improvements were not possible in the previous Black Sea reanalysis, as its closed boundaries required a controlled freshwater balance to prevent drifts in SSH.

Overall, the BLK-REA results are highly satisfactory for key ocean variables, including T, S, SLA. T accuracy exhibits strong seasonality, with the basin-averaged RMSD of SST reaching its lowest value in spring ( $0.43\text{ }^{\circ}\text{C}$ ) and its highest in fall ( $0.61\text{ }^{\circ}\text{C}$ ). At depths within the seasonal thermocline, BLK-REA shows high RMSD errors for T in fall and summer, while errors are lower in winter and spring. In contrast, salinity shows less seasonal variation, with the highest errors consistently occurring in the 50–200 m layer throughout most of the period (Figure 32; bottom-right). Occasionally, salinity errors are also elevated at the surface. SLA errors do not exhibit clear seasonality and have remained around  $0.02\text{ m}$  since 2000; an acceptable level considering that the SLA observation error used in data assimilation is approximately  $0.04\text{ m}$ . Across all seasons, the highest SLA errors are observed along the Rim Current, primarily due to high mesoscale activity along its pathway.

515 The reanalysis has proven to be an important tool for investigating the warming trend in the Black Sea, highlighting the recent  
516 disappearance of the CIL. Both T and OHC exhibit a warming signal. In the 0–100 m layer, the warming trend is occasionally  
517 interrupted, with decreases in OHC coinciding with periods of CIL presence, as observed in 2012, 2017 and 2022 (Figure 109).  
518 Between 1993 and 2010, the decline in CIL formation may have influenced the MOC in the Black Sea. However, further  
519 investigations are needed to understand the recent increase in MOC and its relation with the CIL formation. Our results also  
520 reveal the significant influence of wind stress curl on the interannual variability of the Rim Current, with a particularly strong  
521 signal observed in its southern branch.

522 The BLK-REA dataset presented in this manuscript has been available online in the Copernicus Marine Service catalog since  
523 December 2024 and is extended monthly in Interim mode, which applies less refined configurations for preliminary processing.  
524 The Interim results are replaced annually with an extension of the reanalysis produced using optimal configurations and the  
525 assimilation of reprocessed data, which is considered the highest quality of observations. In alignment with the Black Sea near-  
526 real-time analysis and forecasting system, preparations for the next BLK-REA are already underway. Planned improvements  
527 include the integration of the Azov Sea in the model domain and the inclusion of runoff data from the European Flood  
528 Awareness System (Thielen et al., 2009). The plan also includes extending the reanalysis to cover previous decades, starting  
529 from 1980. This will allow for the extension of the existing OMIs and the preparation of new ones. In fact, tracking the warming  
530 signal in the Black Sea is essential, and our plan is to expand the analysis of the impacts of this warming, including monitoring  
531 marine heatwaves.

532 However, a major challenge is the limited availability of observations from 1980 onward. To address this gap, it may be  
533 necessary to integrate additional in-situ datasets beyond those available from SeaDataNet and Copernicus. Therefore,  
534 continuous monitoring of the Black Sea – particularly by enhancing observation systems – is crucial for maintaining the quality  
535 of reanalysis. In recent years, ongoing advancements in observation technologies and data integration have become  
536 increasingly important to further improve reanalysis accuracy and support long-term environmental studies.

## 537 **5 Data Availability**

538 The BLK-REA dataset presented in this study can be found in online repositories. The names of the repository/repositories  
539 and accession number(s) can be found below: <https://doi.org/10.48670/mds-00356>.

## 540 **6 Author contribution**

541 LL led the study, built the reanalysis system, and was involved in all parts of the work. DA and MI contributed to the  
542 development of the hydrodynamical model. They also shared useful ideas that improved the study in many ways. EJ helped  
543 set up the data assimilation strategies and also gave important suggestions to improve the work. FC helped with the validation  
544 of the reanalysis results. AS gave helpful comments that guided the research. PM supported the preparation of the in-situ

545 observation data for the data assimilation and helped with the validation step. EC also gave useful suggestions that helped  
546 improve the work. All authors contributed to writing the article and approved the final version.

## 547 **7 Competing interests**

548 The authors declare that they have no conflict of interest.

## 549 **8 Acknowledgements**~~Competing interests~~

550 The authors thank Y. Kim and one anonymous referee for their constructive comments that improved the manuscript.

## 551 **98 Financial support**

552 This research was funded by the Copernicus Marine Service for the Black Sea Monitoring and Forecasting Centre (Contract  
553 No. 21002L4-COP-MFC-BS-5400).

## 554 **References**

555 [Altıok, H., and Kayışoğlu, M.: Seasonal and interannual variability of water exchange in the Strait of Istanbul, \*Mediterr. Mar. Sci.\*, 16\(3\), 644–655, 2015.](#)

557 [Beşiktepe, Ş. T., Sur, H. I., Özsoy, E., Latif, M. A., Oğuz, T., and Ünlüata, Ü.: The circulation and hydrography of the Marmara Sea, \*Prog. Oceanogr.\*, 34\(4\), 285–334, 1994.](#)

559 [Capet, A., Vandenbulcke, L., and Grégoire, M.: A new intermittent regime of convective ventilation threatens the Black Sea oxygenation status, \*Biogeosciences\*, 17, 6507–6525, <https://doi.org/10.5194/bg-17-6507-2020>, 2020.](#)

561 [Castellari, S., Pinardi, N., and Leaman, K.: A model study of air-sea interactions in the Mediterranean Sea, \*J. Mar. Syst.\*, 18, 89–114, \[https://doi.org/10.1016/s0924-7963\\(98\\)90007-0\]\(https://doi.org/10.1016/s0924-7963\(98\)90007-0\), 1998.](#)

563 [Chanut, J.: Nesting code for NEMO, Tech. rep., European Union: Marine Environment and Security for the European Area \(MERSEA\) Integrated Project, MERSEA-WP09-MERCA-TASK-9.1.1, 2005.](#)

565 [Ciliberti, S. A., Grégoire, M., Staneva, J., Palazov, A., Coppini, G., Lecci, R., Peneva, E., Matreata, M., Marinova, V., Masina, S., Pinardi, N., Jansen, E., Lima, L., Aydoğdu, A., Creti', S., Stefanizzi, L., Azevedo, D., Causio, S., Vandenbulcke, L., ...](#)

567 Agostini, P.: Monitoring and Forecasting the Ocean State and Biogeochemical Processes in the Black Sea: Recent  
568 Developments in the Copernicus Marine Service, J. Mar. Sci. Eng., 9(10), 1146, <https://doi.org/10.3390/jmse9101146>, 2021.

569 Ciliberti, S. A., Jansen, E., Coppini, G., Peneva, E., Azevedo, D., Causio, S., Stefanizzi, L., Creti', S., Lecci, R., Lima, L.,  
570 Ilicak, M., Pinardi, N., and Palazov, A.: The Black Sea Physics Analysis and Forecasting System within the Framework of the  
571 Copernicus Marine Service, J. Mar. Sci. Eng., 10(1), 48, <https://doi.org/10.3390/jmse10010048>, 2022.

572 Çokacar, T.: Cold Intermediate Water Formation in the Black Sea Triggered by March 2022 Cold Intrusions, J. Mar. Sci. Eng.,  
573 12(11), 2027, <https://doi.org/10.3390/jmse12112027>, 2024.

574 Courtier, P.: Variational methods, J. Meteor. Soc. Japan, 75, 211–218, 1997.

575 Dobricic, S., and Pinardi, N.: An oceanographic three-dimensional variational data assimilation scheme, Ocean Model., 22,  
576 89–105, <https://doi.org/10.1016/j.ocemod.2008.01.004>, 2008.

577 Farina, R., Dobricic, S., Storto, A., Masina, S., and Cuomo, S.: A revised scheme to compute horizontal covariances in an  
578 oceanographic 3D-VAR assimilation system, J. Comput. Phys., 284, 631–647, <https://doi.org/10.1016/j.jcp.2015.01.003>,  
579 2015.

580 Faugère, Y., Taburet, G., Ballarotta, M., Pujol, I., Legeais, J. F., Maillard, G., Durand, C., Dagneau, Q., Lievin, M., Sanchez  
581 Roman, A., and Dibarboure, G.: DUACS DT2021: 28 years of reprocessed sea level altimetry products, EGU General  
582 Assembly 2022, Vienna, Austria, 23–27 May 2022, EGU22-7479, <https://doi.org/10.5194/egusphere-egu22-7479>, 2022.

583 Garcia, H. E., Boyer, T. P., Baranova, O. K., Locarnini, R. A., Mishonov, A. V., Grodsky, A., Paver, C. R., Weathers, K. W.,  
584 Smolyar, I. V., Reagan, J. R., Seidov, D., and Zweng, M. M.: World Ocean Atlas 2018: Product Documentation, A. Mishonov,  
585 Technical Editor, 2019.

586 Good, S., Fiedler, E., Mao, C., Martin, M. J., Maycock, A., Reid, R., Roberts-Jones, J., Searle, T., Waters, J., While, J., and  
587 Worsfold, M.: The Current Configuration of the OSTIA System for Operational Production of Foundation Sea Surface  
588 Temperature and Ice Concentration Analyses, Remote Sens., 12, 720, <https://doi.org/10.3390/rs12040720>, 2020.

589 Gunduz, G., Causio, S., Bonino, G., Vandenbulcke, L., Grégoire, M., Lima, L., Ciliberti, S., Ilicak, M., Aydogdu, A., Masina,  
590 S., Coppini, G., and Pinardi, N.: Coastal upwelling along the Turkish coast of the Black Sea: Its role in the distribution of the  
591 hydrographic properties, J. Oper. Oceanogr., 15:sup1, s205–s211, <https://doi.org/10.1080/1755876X.2022.2095169>, 2022.

592 Haines, K.: Ocean reanalyses, in: New Frontiers in Operational Oceanography, edited by: Chassignet, E., Pascual, A., Tintoré,  
593 J., and Verron, J., Liguria: GODAE OceanView, 545–562, <https://doi.org/10.17125/gov2018.ch19>, 2018.

594 [Ilicak, M., Federico, I., Barletta, I., Mutlu, S., Karan, H., Ciliberti, S. A., et al.: Modeling of the Turkish Strait system using a](#)  
595 [high resolution unstructured grid ocean circulation model, J. Mar. Sci. Eng., 9, 769, <https://doi.org/10.3390/jmse9070769>,](#)  
596 [2021.](#)

597 [Ilicak, M., Causio, S., Ciliberti, S., Coppini, G., Lima, L., Aydogdu, A., Azevedo, D., Lecci, R., Cetin, D. U., Masina, S.,](#)  
598 [Peneva, E., Gunduz, M., and Pinardi, N.: The Black Sea overturning circulation and its indicator of change, J. Oper. Oceanogr.,](#)  
599 [15:sup1, s64–s71, <https://doi.org/10.1080/1755876X.2022.2095169>, 2022.](#)

600 [Ivanov, L. I., Backhaus, J. O., Özsoy, E., and Wehde, H.: Convection in the Black Sea during cold winters, J. Mar. Syst., 31,](#)  
601 [65–76, \[https://doi.org/10.1016/S0924-7963\\(01\\)00047-1\]\(https://doi.org/10.1016/S0924-7963\(01\)00047-1\), 2001.](#)

602 [Ingleby, B., and Huddleston, M.: Quality control of ocean temperature and salinity profiles—Historical and real-time data, J.](#)  
603 [Mar. Syst., 65, 158–175, <https://doi.org/10.1016/j.jmarsys.2005.11.019>, 2007.](#)

604 [Korotaev, G., Oguz, T., Nikiforov, A., and Koblinsky, C.: Seasonal, interannual, and mesoscale variability of the Black Sea](#)  
605 [upper layer circulation derived from altimeter data, J. Geophys. Res. Oceans, 108, 3122, 2003.](#)

606 [Korotaev, G. K., Knysh, V. V., and Kubryakov, A. I.: Study of formation process of cold intermediate layer based on reanalysis](#)  
607 [of Black Sea hydrophysical fields for 1971–1993, Izv. Atmos. Ocean. Phys., 50, 35–48,](#)  
608 [https://doi.org/10.1134/S0001433813060108, 2014.](#)

609 [Kubryakov, A. A., and Stanichny, S. V.: Mesoscale eddies in the Black Sea from satellite altimetry data, Oceanology, 55, 56–](#)  
610 [67, <https://doi.org/10.1134/S0001437015010105>, 2015.](#)

611 [Lima, L., Peneva, E., Ciliberti, S., Masina, S., Lemieux, B., Storto, A., et al.: Copernicus marine service ocean state report,](#)  
612 [issue 4, J. Oper. Oceanogr., 13:sup1, s41–s47, <https://doi.org/10.1080/1755876X.2020.1785097>, 2020.](#)

613 [Lima, L., Ciliberti, S. A., Aydoğdu, A., Masina, S., Escudier, R., Cipollone, A., Azevedo, D., Causio, S., Peneva, E., Lecci,](#)  
614 [R., Clementi, E., Jansen, E., Ilicak, M., Cretì, S., Stefanizzi, L., Palermo, F., and Coppini, G.: Climate Signals in the Black Sea](#)  
615 [From a Multidecadal Eddy-Resolving Reanalysis, Front. Mar. Sci., 8, 710973, <https://doi.org/10.3389/fmars.2021.710973>,](#)  
616 [2021.](#)

617 [Ludwig, W., Dumont, E., Meybeck, M., and Heussner, S.: River discharges of water and nutrients to the Mediterranean and](#)  
618 [Black Sea: major drivers for ecosystem changes during past and future decades?, Prog. Oceanogr., 80, 199–217,](#)  
619 [https://doi.org/10.1016/j.pocean.2009.02.001, 2009.](#)

620 Madec, G., and the NEMO team: NEMO ocean engine, Sci. Notes Clim. Model. Cent., 27,  
621 <https://doi.org/10.5281/zenodo.1464816>, 2019.

622 Miladinova, S., Stips, A., Garcia-Gorriz, E., and Macias Moy, D.: Formation and changes of the Black Sea cold intermediate  
623 layer, Prog. Oceanogr., 167, 11–23, <https://doi.org/10.1016/j.pocean.2018.07.002>, 2018.

624 Mulet, S., Buongiorno Nardelli, B., Good, S., Pisano, A., Greiner, E., Monier, M., et al.: Ocean temperature and salinity, in:  
625 Copernicus Marine Service Ocean State Report, J. Oper. Oceanogr., 11:suppl.1, s13–s16,  
626 <https://doi.org/10.1080/1755876X.2018.1489208>, 2018.

627 Micaletto, G., Barletta, I., Mocavero, S., Federico, I., Epicoco, I., Verri, G., Coppini, G., Schiano, P., Aloisio, G., and Pinardi,  
628 N.: Parallel implementation of the SHYFEM (System of HydroDYNAMIC Finite Element Modules) model, Geosci. Model Dev.,  
629 15, 6025–6046, <https://doi.org/10.5194/gmd-15-6025-2022>, 2022.

630 Myroshnychenko, V., and Simoncelli, S.: SeaDataCloud Temperature and Salinity Historical Data Collection for the Black  
631 Sea (Version 1), Ref. Prod. Info. Doc., SeaDataCloud, <https://doi.org/10.13155/56683>, 2018.

632 Myroshnychenko, V.: SeaDataCloud Temperature and Salinity Historical Data Collection for the Black Sea (Version 2), Ref.  
633 Prod. Info. Doc., SeaDataCloud, <https://doi.org/10.13155/77211>, 2020.

634 Oguz, T., Latun, V. S., Latif, M. A., Vladimirov, V. V., Sur, H. I., Makarov, A. A., Özsoy, E., Kotovshchikov, B. B., Eremeev,  
635 V., and Unluata, U.: Circulation in the surface and intermediate layers of the Black Sea, Deep Sea Res. Part I, 40, 1597–1612,  
636 1993.

637 Oke, P. R., and Sakov, P.: Representation error of oceanic observations for data assimilation, J. Atmos. Oceanic Technol., 25,  
638 1004–1017, <https://doi.org/10.1175/2007jtecho558.1>, 2008.

639 Özsoy, E., and Ünlüata, Ü.: Oceanography of the Black Sea: a review of some recent results, Earth Sci. Rev., 42, 231–272,  
640 [https://doi.org/10.1016/s0012-8252\(97\)81859-4](https://doi.org/10.1016/s0012-8252(97)81859-4), 1997.

641 Peneva, E., Stanev, E., Ciliberti, S., Lima, L., Aydogdu, A., Marinova, V., and Valcheva, N.: Interannual variations of the  
642 Black Sea Rim Current, J. Oper. Oceanogr., 14:sup1, s53–s59, <https://doi.org/10.1080/1755876X.2021.1946240>, 2021.

643 Pettenuzzo, D., Large, W. G., and Pinardi, N.: On the correction of ERA-40 surface flux products consistent with the  
644 Mediterranean heat and water budgets and the connection between basin surface total heat flux and NAO, J. Geophys. Res.,  
645 115, C06022, <https://doi.org/10.1029/2009JC005631>, 2010.

646 Podymov, O. I., Ocherednik, V. V., Silvestrova, K. P., and Zatsepin, A. G.: Upwellings and Downwellings Caused by  
647 Mesoscale Water Dynamics in the Coastal Zone of Northeastern Black Sea, J. Mar. Sci. Eng., 11, 1628,  
648 <https://doi.org/10.3390/jmse11081628>, 2023.

649 Stanev, E. V., Le Traon, P.-Y., and Peneva, E. L.: Sea level variations and their dependency on meteorological and hydrological  
650 forcing: analysis of altimeter and surface data for the Black Sea, J. Geophys. Res., 105(C7), 17203–17216,  
651 <https://doi.org/10.1029/1999JC900318>, 2000.

652 Stanev, E. V., Peneva, E., and Chtirkova, B.: Climate change and regional ocean water mass disappearance: case of the Black  
653 Sea, J. Geophys. Res. Oceans, 124, 4803–4819, <https://doi.org/10.1029/2019JC015076>, 2019.

654 Storto, A., Dobricic, S., Masina, S., and Di Pietro, P.: Assimilating along-track altimetric observations through local  
655 hydrostatic adjustment in a global ocean variational assimilation system, Mon. Weather Rev., 139, 738–754,  
656 <https://doi.org/10.1175/2010mwr3350.1>, 2011.

657 Szekely, T., Gourrion, J., Pouliquen, S., and Reverdin, G.: CORA, Coriolis Ocean Dataset for Reanalysis, SEANOE,  
658 <https://doi.org/10.17882/46219>, 2024.

659 Thielen, J., Bartholmes, J., Ramos, M. H., and De Roo, A.: The European flood alert system—part 1: concept and development,  
660 Hydrol. Earth Syst. Sci., 13(2), 125–140, 2009.

661 Yang, C., and Coauthors: Gathering Users and Developers to Shape Together the Next-Generation Ocean Reanalyses, Bull.  
662 Amer. Meteor. Soc., 106, E419–E429, <https://doi.org/10.1175/BAMS-D-24-0034.1>, 2025.

663 Altioek, H., and Kayışoğlu, M. (2015). Seasonal and interannual variability of water exchange in the Strait of Istanbul.  
664 Mediterranean Marine Science, 16(3), 644–655.

665 Beşiktepe, Ş. T., Sur, H. I., Özsoy, E., Latif, M. A., Oğuz, T., & Ünlüata, Ü. (1994). The circulation and hydrography of the  
666 Marmara Sea. Progress in Oceanography, 34(4), 285–334.

667 Capet, A., Vandenbuleke, L., and Grégoire, M.: A new intermittent regime of convective ventilation threatens the Black Sea  
668 oxygenation status, Biogeosciences, 17, 6507–6525, <https://doi.org/10.5194/bg-17-6507-2020>, 2020.

669 Castellari, S., Pinardi, N., and Leaman, K. (1998). A model study of air-sea interactions in the Mediterranean Sea. J. Mar. Sys.  
670 18, 89–114. doi: 10.1016/s0924-7963(98)90007-0

671 Chanut, J., 2005: Nesting code for nemo. Tech. rep., European Union: Marine Environment and Security for the European  
672 Area (MERSEA) Integrated Project. MERSEA-WP09-MERCA-TASK-9.1.1.

673 Ciliberti, S. A., Grégoire, M., Staneva, J., Palazov, A., Coppini, G., Lecce, R., Peneva, E., Matreata, M., Marinova, V., Masina,  
674 S., Pinardi, N., Jansen, E., Lima, L., Aydoğdu, A., Creti, S., Stefanizzi, L., Azevedo, D., Causio, S., Vandenbuleke, L., ...

675 Agostini, P. (2021). Monitoring and Forecasting the Ocean State and Biogeochemical Processes in the Black Sea: Recent  
676 Developments in the Copernicus Marine Service. *Journal of Marine Science and Engineering*, 9(10), 1146.  
677 <https://doi.org/10.3390/jmse9101146>

678 Ciliberti, S. A., Jansen, E., Coppini, G., Peneva, E., Azevedo, D., Causio, S., Stefanizzi, L., Creti', S., Lecci, R., Lima, L.,  
679 Ilicak, M., Pinardi, N., & Palazov, A. (2022). The Black Sea Physics Analysis and Forecasting System within the Framework  
680 of the Copernicus Marine Service. *Journal of Marine Science and Engineering*, 10(1), 48.  
681 <https://doi.org/10.3390/jmse10010048>

682 Çokacar, T. (2024). Cold Intermediate Water Formation in the Black Sea Triggered by March 2022 Cold Intrusions. *Journal*  
683 *of Marine Science and Engineering*, 12(11), 2027. <https://doi.org/10.3390/jmse12112027>

684 Courtier, P. (1997). Variational methods. *J. Meteor. Soc. Japan* 75, 211–218.

685 Dobricic, S., and Pinardi, N. (2008). An oceanographic three-dimensional variational data assimilation scheme. *Ocean Model.*  
686 22, 89–105. doi: 10.1016/j.ocemod.2008.01.004

687 Faugère, Y., Taburet, G., Ballarotta, M., Pujol, I., Legeais, J. F., Maillard, G., Durand, C., Dagneau, Q., Lievin, M., Sanchez  
688 Roman, A., and Dibarboure, G.: DUACS DT2021: 28 years of reprocessed sea level altimetry products, EGU General  
689 Assembly 2022, Vienna, Austria, 23–27 May 2022, EGU22-7479, <https://doi.org/10.5194/egusphere-egu22-7479>, 2022.

690 Ingleby, B., and Huddleston, M. (2007). Quality control of ocean temperature and salinity profiles—Historical and real-time  
691 data. *J. Mar. Syst.* 65, 158–175. doi: 10.1016/j.jmarsys.2005.11.019

692 Ivanov, L.I., Baekhaus, J.O., Özsoy, E., Wehde, H., 2001. Convection in the Black Sea during cold winters. *J. Mar. Syst.* 31,  
693 65–76. [https://doi.org/10.1016/S0924-7963\(01\)00047-1](https://doi.org/10.1016/S0924-7963(01)00047-1).

694 Garcia H.E., T.P. Boyer, O.K. Baranova, R.A. Locarnini, A.V. Mishonov, A. Grodsky, C.R. Paver, K.W. Weathers, I.V.  
695 Smolyar, J.R. Reagan, D. Seidov, M.M. Zweng (2019). *World Ocean Atlas 2018: Product Documentation*. A. Mishonov,  
696 Technical Editor.

697 Farina, R., Dobricic, S., Storto, A., Masina, S., and Cuomo, S. (2015). A revised scheme to compute horizontal covariances in  
698 an oceanographic 3D-VAR assimilation system. *J. Comput. Phys.* 284, 631–647. doi: 10.1016/j.jcp.2015.01.003

699 Good, S., Fiedler, E., Mao, C., Martin, M.J., Maycock, A., Reid, R., Roberts-Jones, J., Searle, T., Waters, J., While, J.,  
700 Worsfold, M. The Current Configuration of the OSTIA System for Operational Production of Foundation Sea Surface  
701 Temperature and Ice Concentration Analyses. *Remote Sens.* 2020, 12, 720, doi:10.3390/rs12040720.

702 Gunduz, G., Causio, S., Bonino, G., Vandenbulcke, L., Gregorie, M., Lima, L., Ciliberti, S., Ilicak, M., Aydogdu, A., Masina,  
703 S., Coppini, G., and Pinardi, N. (2022). Coastal upwelling along the Turkish coast of the Black Sea: Its role in the distribution  
704 of the hydrographic properties. In: Copernicus Ocean State Report, issue 6, *Journal of Operational Oceanography*, 15:sup1,  
705 s205:s211; DOI: [doi.org/10.1080/1755876X.2022.2095169](https://doi.org/10.1080/1755876X.2022.2095169)

706 Haines, K. (2018). “Ocean reanalyses,” in *New Frontiers in Operational Oceanography*, eds E. Chassignet, A. Pascual, J.  
707 Tintoré, and J. Verron (Liguria: GODAE OceanView), 545–562. doi: 10.17125/gov2018.ch19

708 Ilıcak, M., Federico, I., Barletta, I., Mutlu, S., Karan, H., Ciliberti, S. A., et al. (2021). Modeling of the Turkish Strait System  
709 using a high-resolution unstructured grid ocean circulation model. *J. Mar. Sci. Eng.* 9:769. doi: 10.3390/jmse9070769

710 Ilıcak, M., Causio, S., Ciliberti, S., Coppini, G., Lima, L., Aydogdu, A., Azevedo, D., Lecci, R., Cetin, D. U., Masina, S.,  
711 Peneva, E., Gunduz, M., Pinardi, N. (2022). The Black Sea overturning circulation and its indicator of change. In: Copernicus  
712 Ocean State Report, issue 6, Journal of Operational Oceanography, 15:sup1, s64:s71; DOI:  
713 doi.org/10.1080/1755876X.2022.2095169

714 Korotaev, G., Oguz, T., Nikiforov, A., and Koblinsky, C. (2003). Seasonal, interannual, and mesoscale variability of the Black  
715 Sea upper layer circulation derived from altimeter data. *J. Geophys. Res. Oceans* 108:3122.

716 Korotaev, G.K., Knysh, V.V. & Kubryakov, A.I. Study of formation process of cold intermediate layer based on reanalysis of  
717 Black Sea hydrophysical fields for 1971–1993. *Izv. Atmos. Ocean. Phys.* 50, 35–48 (2014).  
718 https://doi.org/10.1134/S0001433813060108

719 Kubryakov, A.A., Stanichny, S.V. Mesoscale eddies in the Black Sea from satellite altimetry data. *Oceanology* 55, 56–67  
720 (2015). https://doi.org/10.1134/S0001437015010105

721 Lima, L., Peneva, E., Ciliberti, S., Masina, S., Lemieux, B., Storto, A., et al. (2020). Copernicus marine service ocean state  
722 report, issue 4. *J. Oper. Oceanogr.* 13(Sup1.), s41–s47. doi: 10.1080/1755876X.2020.1785097

723 Lima, L., Ciliberti, S. A., Aydoğdu, A., Masina, S., Escudier, R., Cipollone, A., Azevedo, D., Causio, S.; Peneva, E., Lecci,  
724 R.; Clementi, E., Jansen, E., Ilıcak, M.; Cretì S., Stefanizzi, L., Palermo, F., & Coppini, G. (2021) Climate Signals in the Black  
725 Sea From a Multidecadal Eddy-Resolving Reanalysis. *Front. Mar. Sci.* 8:710973. doi: 10.3389/fmars.2021.710973.

726 Ludwig, W., Dumont, E., Meybeck, M., and Heussner, S. (2009). River discharges of water and nutrients to the Mediterranean  
727 and Black Sea: major drivers for ecosystem changes during past and future decades? *Prog. Oceanogr.* 80, 199–217. doi:  
728 10.1016/j.pocean.2009.02.001

729 Madec, Gurvan and the NEMO team, (2019). NEMO ocean engine. Scientific Notes of Climate Modelling Center, 27—ISSN  
730 1288-1619, Institut Pierre-Simon Laplace (IPSL), doi:10.5281/zenodo.1464816

731 Miladinova, S., Stips, A., Garcia-Gorriz, E., Macias Moy, D., (2018) Formation and changes of the Black Sea cold intermediate  
732 layer, *Progress in Oceanography*, 167, 11–23, https://doi.org/10.1016/j.pocean.2018.07.002.

733 Mulet, S., Buongiorno Nardelli, B., Good, S., Pisano, A., Greiner, E., Monier, M., et al. (2018). Ocean temperature and salinity.  
734 In: copernicus marine service ocean state report. *J. Oper. Oceanogr.* 11(suppl. 1), s13–s16. doi:  
735 10.1080/1755876X.2018.1489208

736 Micaletto, G., Barletta, I., Moeviero, S., Federico, I., Epicoco, I., Verri, G., Coppini, G., Schiano, P., Aloisio, G., and Pinardi,  
737 N. (2022). Parallel implementation of the SHYFEM (System of Hydrodynamic Finite Element Modules) model, *Geosci.  
738 Model Dev.*, 15, 6025–6046, https://doi.org/10.5194/gmd-15-6025-2022

739 Myroshnychenko Volodymyr, Simonecelli Simona (2018). SeaDataCloud Temperature and Salinity Historical Data Collection  
740 for the Black Sea (Version 1). Ref. Product Information Document (PIDoc). SeaDataCloud. https://doi.org/10.13155/56683

741 ~~Myroshnychenko Volodymyr (2020). SeaDataCloud Temperature and Salinity Historical Data Collection for the Black Sea~~  
742 ~~(Version 2). Ref. Product Information Document (PIDoc). SeaDataCloud. <https://doi.org/10.13155/77211>~~

743 ~~Oguz, T., V. S. Latun, M. A. Latif, V. V. Vladimirov, H. I. Sur, A. A. Makarov, E. Ozsoy, B. B. Kotovshchikov, V. Eremeev,~~  
744 ~~and U. Unluata, Circulation in the surface and intermediate layers of the Black Sea, Deep Sea Res., Part I, 40, 1597–1612,~~  
745 ~~1993.~~

746 ~~Oke, P. R., and Sakov, P. (2008). Representation error of oceanic observations for data assimilation. J. Atmos. Oceanic~~  
747 ~~Technol. 25, 1004–1017. doi: 10.1175/2007jtecho558.1~~

748 ~~Özsoy, E., and Ünlüata, Ü. (1997). Oceanography of the Black Sea: a review of some recent results. Earth Sci. Rev. 42, 231–~~  
749 ~~272. doi: 10.1016/s0012-8252(97)81859-4~~

750 ~~Peneva, E., Stanev, E., Ciliberti, S., Lima, L., Aydogdu, A., Marinova, V., and Valcheva, N. (2021). Interannual variations of~~  
751 ~~the Black Sea Rim Current. In: Copernicus Marine Service Ocean State Report, issue 5, Journal of Operational Oceanography,~~  
752 ~~14:sup1, s53:s59; DOI: 10.1080/1755876X.2021.1946240~~

753 ~~Pettenuzzo, D., Large, W. G., and Pinardi, N. (2010). On the correction of ERA-40 surface flux products consistent with the~~  
754 ~~Mediterranean heat and water budgets and the connection between basin surface total heat flux and NAO. J. Geophys. Res.~~  
755 ~~115:C06022. doi: 10.1029/2009JC005631~~

756 ~~Podymov, O.I.; Ocherednik, V.V.; Silvestrova, K.P.; Zatsepin, A.G. Upwellings and Downwellings Caused by Mesoscale~~  
757 ~~Water Dynamics in the Coastal Zone of Northeastern Black Sea. J. Mar. Sci. Eng. 2023, 11, 1628.~~  
758 ~~<https://doi.org/10.3390/jmse11081628>~~

759 ~~Stanev, E.V., Le Traon, P.-Y., Peneva, E.L. 2000. Sea level variations and their dependency on meteorological and hydrological~~  
760 ~~forcing: analysis of altimeter and surface data for the Black Sea. J. Geophys. Res. 105(C7):17203–17216. doi:~~  
761 ~~<https://doi.org/10.1029/1999JC900318>~~

762 ~~Stanev, E. V., Peneva, E., and Chtirkova, B. (2019). Climate change and regional ocean water mass disappearance: case of the~~  
763 ~~Black Sea. J. Geophys. Res. Oceans 124, 4803–4819. doi: 10.1029/2019JC015076~~

764 ~~Storto, A., Dobricic, S., Masina, S., and Di Pietro, P. (2011). Assimilating along-track altimetric observations through local~~  
765 ~~hydrostatic adjustment in a global ocean variational assimilation system. Mon. Weather Rev. 139, 738–754. doi:~~  
766 ~~10.1175/2010mwr3350.1~~

767 ~~Szekely Tanguy, Gourrion Jerome, Pouliquen Sylvie, Reverdin Gilles (2024). CORA, Coriolis Ocean Dataset for Reanalysis.~~  
768 ~~SEANOE. <https://doi.org/10.17882/46219>~~

769 ~~Thielen, J., Bartholmes, J., Ramos, M. H., & De Roo, A. (2009). The European flood alert system part 1: concept and~~  
770 ~~development. Hydrology and Earth System Sciences, 13(2), 125–140.~~

771 ~~Yang, C., and Coauthors, 2025: Gathering Users and Developers to Shape Together the Next-Generation Ocean Reanalyses.~~  
772 ~~Bull. Amer. Meteor. Soc., 106, E419–E429, <https://doi.org/10.1175/BAMS-D-24-0034.1>~~

773